Variability of quasilinear diffusion coefficients for plasmaspheric hiss

Article

Accepted Version

Variability of Quasilinear Diffusion Coefficients for Plasmaspheric Hiss

C. E. J. Watt[1], H. J. Allison[2,3,4], N. P. Meredith[2], R. L. Thompson[5], S. N. Bentley[1], I. J. Rae[6], S. A. Glauert[2], R. B. Horne[2]

[1]Department of Meteorology, University of Reading, Reading, UK
[2]British Antarctic Survey, Cambridge, UK
[3]Department of Applied Mathematics and Theoretical Physics, University of Cambridge, UK
[4]now at GFZ German Research Centre for Geosciences, Potsdam, Germany
[5]Department of Mathematics and Statistics, University of Reading, Reading, UK
[6]Mullard Space Science Laboratory, University College London, UK

Key Points:

- We construct distributions of quasilinear diffusion coefficients for hiss using multiple simultaneous observations of input parameters
- Using realistic, observed variation of input parameters, diffusion coefficients at a specified energy exhibit large variance
- Distributions of diffusion coefficients are non-Gaussian, including when parameterized by specified ranges of AE-index

Corresponding author: Clare Watt, `c.e.watt@reading.ac.uk`

Abstract

In the Outer Radiation Belt, the acceleration and loss of high-energy electrons is largely controlled by wave-particle interactions. Quasilinear diffusion coefficients are an efficient way to capture the small-scale physics of wave-particle interactions due to magnetospheric wave modes such as plasmaspheric hiss. The strength of quasilinear diffusion coefficients as a function of energy and pitch-angle depends on both wave parameters and plasma parameters such as ambient magnetic field strength, plasma number density and composition. For plasmaspheric hiss in the magnetosphere, observations indicate large variations in the wave intensity and wavenormal angle, but less is known about the simultaneous variability of the magnetic field and number density. We use in-situ measurements from the Van Allen Probe mission to demonstrate the variability of selected factors that control the size and shape of pitch-angle diffusion coefficients: wave intensity, magnetic field strength and electron number density. We then compare with the variability of diffusion coefficients calculated individually from co-located and simultaneous groups of measurements. We show that the distribution of the plasmaspheric hiss diffusion coefficients is highly non-Gaussian with large variance, and that the distributions themselves vary strongly across the three phase-space bins studied. In most bins studied, the plasmaspheric hiss diffusion coefficients tend to increase with geomagnetic activity, but our results indicate that new approaches that include natural variability may yield improved parameterizations. We suggest methods like stochastic parameterization of wave-particle interactions could use variability information to improve modelling of the Outer Radiation Belt.

Plain Language Summary

The electrons in Earth's Radiation Belts exist in a highly rarefied part of space where collisions between particles is very rare. The only way in which the energy or direction of the trapped high-energy electrons can be changed is through interactions with electromagnetic waves. The efficacy of the interaction is a function of the energy and direction of travel of the electrons. In physics-based models of the Radiation belts, the efficacy of the wave-particle interactions is captured in diffusion coefficients. These functions are constructed from information about the amplitude and frequency properties of the waves in the interaction, and the magnetic field strength, ion composition and density of the local plasma. We build up collections of observations of these properties from multiple passes of one of the NASA Van Allen probes through the same three small regions of space. The observations display significant temporal variability. We report on the statistical distributions of wave intensity, magnetic field strength and plasma number density, and investigate the statistical distribution of the resulting diffusion coefficient. We find that the diffusion coefficients are highly variable and suggest that, by borrowing methods from other branches of geophysics such as numerical weather prediction, we may be able to include this variability in our models and improve the performance of Radiation Belt simulations.

1 Introduction

The radiation belts in the terrestrial magnetosphere are regions of high-energy trapped particles in near-Earth space. The inner belt is relatively stable and dominated by high-energy protons. The outer radiation belt exhibits strong variations in both the flux of high-energy electrons and in the extent of the region they inhabit (e.g. Miyoshi, Jordanova, Morioka, and Evans (2005)). A large contributor to the existence of the slot region between the belts (e.g. Meredith, Horne, Glauert, and Anderson (2007); Kim, Shprits, Subbotin, and Ni (2011)), and the rapid variations in the outer belt is wave-particle interactions across a wide range of frequencies (e.g. Thorne (2010); Horne, Meredith, Glauert, and Kersten (2016)). The challenge for modelling wave-particle interactions is that we

would like to construct a model of electron behaviour over hours, days and months when the underlying wave-particle interactions occur on timescales of microseconds to minutes. A powerful method of describing wave particle interactions over long timescales is the use of quasilinear theory to construct diffusion coefficients to encapsulate the micro-scale phsyics (e.g. Horne et al. (2005a)), before using these diffusion coefficients in macro-scale models (e.g. Horne et al. (2005b); Varotsou et al. (2008); Subbotin and Shprits (2009); Reeves et al. (2012); Glauert, Horne, and Meredith (2014a); Ma et al. (2015); Albert, Starks, Horne, Meredith, and Glauert (2016)). In these types of models, the diffusion coefficients can be considered to be descriptions of "sub-grid scale physics" and contain information regarding the strength of the wave-particle interaction as a function of energy E and pitch-angle α.

Diffusion coefficients D_{ij} can be constructed for interactions between electrons and waves across a wide range of frequencies important in the magnetosphere, from large-scale ultra-low frequency (ULF) waves (e.g. Fei, Chan, Elkington, and Wiltberger (2006); Lejosne, Boscher, Maget, and Rolland (2012); Ozeke, Mann, Murphy, Rae, and Milling (2014)) to higher frequency waves such as electromagnetic ion cyclotron waves (e.g. Kersten et al. (2014); Drozdov et al. (2017)) and whistler-mode waves (e.g. Ni, Thorne, Shprits, and Bortnik (2008); Albert, Meredith, and Horne (2009); Horne et al. (2013); Glauert, Horne, and Meredith (2013); Ripoll et al. (2016)). The diffusion coefficients depend strongly upon wave intensity, but also on parameters that can affect the efficiency and location in (E, α) space of the wave-particle interaction, such as frequency, wavenormal angle, local number density, composition, and ambient magnetic field strength.

Wave characteristics in the magnetosphere are highly variable across a wide range of different wave modes important for the radiation belts. The amplitude of whistler mode waves (Agapitov et al., 2013; Spasojevic et al., 2015; Malaspina et al., 2017; Watt et al., 2017) and the amplitude of ultra-low frequency (ULF) waves (Bentley et al., 2018a) demonstrate significant variability, even when binned by geomagnetic activity or other driving parameter. The wavenormal angle (Agapitov et al., 2013; Hartley et al., 2018) of whistler-mode waves, and the azimuthal wavenumber of ULF waves (Murphy et al., 2018) is also highly variable. Finally, the wave frequency range of whistler-mode waves has demonstrated variability (Meredith et al., 2007; Horne et al., 2013; Li et al., 2015). Additionally, it is important to remember that it is not only the wave characteristics that determine the strength of the wave-particle interaction (Horne et al., 2003b). For example, there is observational evidence that the efficiency of the electromagnetic ion-cyclotron wave-particle interaction can vary with time due to the variation in cold plasma number density, in addition to the variation in the wave properties (Blum et al., 2015).

Typically, diffusion coefficient models use average values of the wave characteristics, and augment these with models of the ambient magnetic field, plasma composition and number density (e.g. Subbotin and Shprits (2009); Fok et al. (2011); Glauert et al. (2013); Horne et al. (2013); Tu et al. (2013)). Models are constructed in phase-space, where a convenient co-ordinate system is based upon the adiabatic invariants μ, J and L^*. Diffusion coefficients are constructed by obtaining bounce- and drift-averaged models of the wave-particle interaction that are constrained by observations. While parameterized diffusion coefficients are generally adequate for understanding the overall dynamics of the radiation belts (e.g. Glauert, Horne, and Meredith (2018)), recent work has shown that event-specific diffusion coefficients can be used to examine specific intervals with greater success (Tu et al., 2014; Ripoll et al., 2016; Mann et al., 2016; Ripoll et al., 2017; Ma et al., 2018). It is important to note that the success of event-specific diffusion coefficient models highlights the large variability of wave-particle interactions possible in the radiation belts, and motivates our attempt to capture, describe and use this variability in future diffusion-based models.

The creation of event-specific diffusion models can capture extreme values and rapid variations that are not reproduced by the averaged parameterized models, however there

are some caveats to their use. Diffusion of drifting electrons in the radiation belts is a global phenomenon, and information regarding wave-particle interactions is required at all magnetic local times (MLT) in order to estimate the drift-averaged diffusion coefficient. If one uses a small number of spacecraft to construct an event-specific diffusion model, then that model will not capture all of the variability in MLT and may result in under- or over-estimating the diffusion that results. More pressing is the knowledge that the NASA Van Allen Probes and JAXA Arase spacecraft are missions with finite lifetimes, and so event-specific information will not always be available in future, or for studying historical events prior to their launch. A parameterized model of diffusion coefficients therefore remains a valid goal.

We suggest that given the inherent variability of wave-particle interactions in the radiation belts, a modelling strategy such as stochastic parameterization (e.g. Berner et al. (2017)) is worth consideration. In these types of models, the parameterization of the diffusion coefficients is not deterministic, but probabilistic, and the variability of the wave-particle interactions is rigorously included. To apply a stochastic parameterization to wave-particle interactions in the radiation belts, we first need to characterize all aspects of variability of the diffusion coefficients for each wave mode: the underlying distribution of the variability, the size of the variance, the characteristic scales of temporal and spatial variability and the existence of any caps or upper limits to diffusion. In this paper, we use observations from Van Allen probes to investigate the variability of diffusion due to plasmaspheric hiss. We will demonstrate the variability of the input parameters for the calculation of the diffusion coefficient, and discuss the variability of a set of diffusion coefficients calculated from co-located and simultaneous measurements in small phase-space bins in the inner magnetosphere. We attempt to broadly identify the underlying distribution of each of the quantities we study, as well as estimate the size of the variability. Note that probabilistic models can be created quite efficiently if the underlying distribution is well-defined (e.g. normal or log-normal), since a small number of parameters (e.g. mean and standard deviation or their equivalent) can be used to characterize the entire distribution.

We focus on plasmaspheric hiss as it is a wave mode ubiquitous to the high density regions of the plasmasphere. It is straightforwardly identified in spacecraft observations of electromagnetic wave spectra, with frequencies from tens of Hz to a few kHz (Li et al., 2015) that does not tend to feature rapid temporal structures in frequency spectra (e.g. Li, Thorne, Bortnik, Tao, and Angelopoulos (2012)). Plasmaspheric hiss is important for losses of high-energy electrons in the inner magnetosphere through pitch-angle scattering (Meredith et al., 2006; Lam et al., 2007), and particularly for loss in the slot region (Meredith et al., 2007, 2009). Velocity-space diffusion due to plasmaspheric hiss is dominated by pitch-angle diffusion (Lyons et al., 1972) and so we study the variability of the pitch-angle diffusion coefficient $D_{\alpha\alpha}$ in this paper.

In this work, we use data from multiple instruments on board the NASA Van Allen Probes mission to quantify the range of pitch-angle diffusion coefficients active in the inner magnetosphere due to plasmaspheric hiss and relate them to diffusion coefficient values calculated from the means or medians of the input parameters, such as plasma to gyro-frequency ratio, and wave intensity. We examine the underlying distributions of each input parameter, as well as the distribution of the resulting pitch-angle diffusion coefficients, and determine how varying each input parameter varies the diffusion coefficient. We will also determine how the probability distribution of hiss-mediated pitch-angle diffusion coefficients varies with increasing geomagnetic activity, since activity is often used to parameterize wave-particle interactions in the radiation belts (e.g. Horne et al. (2013)). In Section 2 we discuss the data sources and methods we will use to characterize the variability of inputs to and outputs of the diffusion coefficient calculation using the British Antarctic Survey PADIE code (Glauert & Horne, 2005). Section 3 demonstrates the variability of the inputs independently, before we show the variability of the resulting dif-

fusion coefficients in Section 4. We discuss the implications of results for modeling wave-particle interactions in the radiation belts in Section 5, and conclude in Section 6.

2 Data and Methods

2.1 Input parameters

We use simultaneous and co-located data from different instruments on the NASA Van Allen Probes mission to study the distribution of quasilinear diffusion coefficients. Our intention here is to illustrate, using a few examples, the variability that may be present in diffusion coefficients due to plasmaspheric hiss, and to evaluate whether our analysis should be extended in future work. It is important to note that the calculation of diffusion coefficients is computationally expensive, and so we choose a small number of example bins in this illustrative study. We select three small bins in the inner magnetosphere that are predominantly inside the plasmasphere and in the morning sector, where hiss has been shown to be present (Meredith et al., 2004, 2018). It's equally important to note that the extent of the phase-space bin used to collate observations when constructing a diffusion model is a source of potential variability; too large a bin, and we run the risk of conflating wave activity and plasma properties from different regions of the magnetosphere, whereas too small a bin can lead to small numbers of observations and a statistically poor sample. Thanks to the excellent coverage of the Van Allen probes over the $>$ 3 year period used, we have $>$ 1500 data points in each of the relatively small bins used (see description below). We hope to minimise any potential variations due to radial and azimuthal location, and note that future, more comprehensive, models can help determine the most appropriate resolution, or indeed coordinate system, to use when building an observationally-constrained diffusion coefficient model.

We choose a phase-space coordinate system that is tied to electron adiabatic behaviour in the magnetosphere, i.e. we bin our observations in L^* where it has been calculated using the Olson-Pfitzer quiet time model (Olson & Pfizer, 1977) with the International Geomagnetic Reference Field (IGRF) for the middle of the appropriate year. Since L^* is defined for particles, but we here use it for waves, we assume a local pitch angle of $\alpha = 90^\circ$ for this calculation. We also restrict our observations to those that are in a small section of magnetic local time (MLT) and magnetic latitude λ_m (where $\lambda_m = 0$ at the magnetic equator). We focus on plasmaspheric hiss and so choose three L^* ranges that are predominantly inside the plasmasphere: $2.45 < L^* < 2.55$, $2.95 < L^* < 3.05$ and $3.45 < L^* < 3.55$ (these bins will be referred to as the $L^* = 2.5$ bin, the $L^* = 3.0$ bin and the $L^* = 3.5$ bin, respectively). Narrow bin sizes are chosen in an attempt to minimize any variation of diffusion coefficient with L^*. Similarly, we choose a narrow range of 0900-1000 MLT for all three regions, and a narrow range of magnetic latitude $0 < \lambda_m < 6^\circ$, as wave and plasma parameters are known to be MLT and latitude dependent (Meredith et al., 2004, 2018).

Our aim is to use co-located and simultaneous measurements of key inputs for the diffusion coefficient calculation in order to determine the variability of diffusion in each chosen plasmaspheric bin. Ripoll et al. (2017) have recently demonstrated the importance of using such simultaneous observations of multiple input parameters in order to more accurately determine the quasilinear diffusion coefficients during specific events. Coefficients for the interaction between plasmaspheric hiss and electrons (e.g. equations (11-13) in Glauert and Horne (2005)) depend upon the local magnetic field strength $|B|$ (through the electron gyrofrequency $\Omega_e = |q_e||B|/m_e$) and the local electron number density n_e (through the electron plasma frequency $\omega_{pe} = (n_e q_e^2/\epsilon_0 m_e)^{1/2}$). Here, q_e and m_e are the electron charge and mass, respectively, and ϵ_0 is the electric permittivity of free space. They also depend upon the intensity of the waves δB^2, and the dependence of the intensity on frequency ω and wavenormal angle ψ. In order to simplify our analysis for our initial study of the variability of quasilinear diffusion coefficients, we will fo-

cus on the impact of variability in two important input parameters: wave intensity δB^2 and the ratio of plasma to gyrofrequency $\omega_{pe}/\Omega_e = f_{pe}/f_{ce}$, where $f_{pe} = \omega_{pe}/(2\pi)$ and $f_{ce} = \Omega_e/(2\pi)$. We therefore fix the shape of the input wave spectra, and vary only the wave intensity at $f = 252$ Hz. This frequency is chosen as it is close to the peak of the statistical average wave spectra as determined by Li et al. (2015). We stress that it is very important to use co-located and simultaneous measurements of input parameters in order to capture the true variability of diffusion coefficients (c.f. Ripoll et al. (2017)). Future work will consider the effects of variability in the observed dependence of δB^2 on ω and ψ, the local ion composition, and the dependence of input wave parameters on magnetic latitude.

For this study we used data from the Van Allen probe A. The Van Allen probes were launched on 30 August 2012 into highly elliptical orbits with a perigee of 618 km, an apogee of 30,414 km and an inclination of 10.2°. The orbital period is 537.1 minutes. The satellites sweep through the plasmasphere approximately 5 times per day, making them excellent probes of this important region.

We use data from the Electric and Magnetic Field Instrument Suite and Integrated Science (EMFISIS)(Kletzing et al., 2013) on board Van Allen probe A. We use the Waveform Receiver (WFR) for measurements of the wave magnetic field. This instrument provides measurements of all three components of the wave electric and magnetic fields in 65 frequency channels in the frequency range from 10 Hz to $\sim$ 12 kHz every 6 seconds. Specifically we use the WNA survey data product for the sum of the three components of the wave magnetic field and the ellipticity. Concomitant measurements of the electron gyrofrequency f_{ce} are determined from the 1s fluxgate magnetometer data. The co-located measurements of the electron plasma frequency are determined from the High Frequency Receiver (HFR). This instrument provides measurements of one component of the electric field in the plane perpendicular to the spin axis in 82 logarithmically-spaced frequency bins in the frequency range 10-400 kHz every 6s. The electron plasma frequency f_{pe}, which is provided as a L4 density product, is derived from the lower hybrid resonance frequency when visible, or the lower frequency limit of the continuum radiation (Kurth et al., 2015).

Many wave parameters are required as input for the diffusion coefficient (see e.g. Glauert and Horne (2005)). However, we model the variability of the waves using only one variable - the intensity of emission at $f = 252$ Hz which is used to constrain the peak of the frequency distribution in the diffusion coefficient calculation (see section 2.2). Li et al. (2015) demonstrate that the statistical hiss frequency spectrum peaks at this frequency for low L.

To compile the subset of data required in our study, we sequentially analyzed each day of Van Allen probe A data from 15 September 2012 until 12 February 2016. We stored co-located measurements of plasmaspheric hiss wave power spectral density at $f = 252$ Hz, f_{ce}, f_{pe}, UT date and time, magnetic latitude, magnetic local time and geomagnetic activity as monitored by the AE index as a function of half orbit, L^*, in steps of $0.1L^*$, and observation number in that bin. For our chosen location bins we then extracted and stored each co-located measurement of the wave power spectral density at $f = 252$ Hz, f_{pe}, f_{ce} and the corresponding AE index. These measurements are used to first construct probability density functions of the input parameters for the diffusion coefficient calculation f_{pe}/f_{ce} and wave intensity, and the probability distributions of the underlying physical parameters like magnetic field and number density that feed into the input f_{pe}/f_{ce} ratio (see section 3). Diffusion coefficients are then calculated using the method described in section 2.2 and their probability distributions displayed in section 4.

Note that plasmaspheric hiss can overlap in frequency with magnetosonic waves (Russell et al., 1970; Santolík et al., 2004) and whistler mode chorus (Koons & Roeder, 1990; Tsurutani & Smith, 1977). We excluded periods of magnetosonic waves, which typ-

ically have large wave normal angles and hence low ellipticity values, by excluding waves with ellipticity less than 0.7. Plasmaspheric hiss tends to be confined to high-density regions associated with the plasmasphere (e.g., Thorne, Smith, Burton, and Holzer (1973)) and plasmaspheric plumes (e.g., Summers et al. (2008)), whereas whistler mode chorus waves are largely confined to the low-density region of the plasma trough (Tsurutani & Smith, 1977; Meredith et al., 2001). We further excluded probable observations of whistler mode chorus by restricting the co-located measurements to those observed inside the plasmapause. We applied the number density threshold adopted by Sheeley, Moldwin, Rassoul, and Anderson (2001) to separate measurements likely made inside the plasmasphere, and those likely made outside. Figure 1 shows the distribution of observations in f_{pe} and f_{ce} for each of the three volume bins studied. The solid line indicates the number density threshold used by Sheeley et al. (2001). In Figure 1, observations that lie above each modeled line are deemed to be inside the plasmasphere, and are used in the subsequent analysis. Over the ~ 3.5 years of Van Allen Probes coverage used in this study from 15 September 2012 until 12 February 2016, this provides us with 1570 points in the $L^* = 2.5$ bin, 2377 in the $L^* = 3.0$ bin, and 3272 in the $L^* = 3.5$ bin.

Figure 1: Occurrence of observations of plasma frequency and plasma gyrofrequency in different regions of the inner magnetosphere. Color indicates number of observations, horizontal dashed line indicates a condition on the number density for measurements inside (above) and outside (below) the plasmapause. (a) $L^* = 2.5$ bin, (b) $L^* = 3.0$ bin and (c) $L^* = 3.5$ bin

2.2 Diffusion coefficient calculation

We use the Pitch Angle and Energy Diffusion of Ions and Electrons (PADIE) code (Glauert & Horne, 2005) in order to calculate bounce-averaged pitch-angle scattering diffusion coefficients $D_{\alpha\alpha}$ for each of our pairs of co-located measurements. PADIE calculates relativistic quasi-linear pitch-angle and energy diffusion coefficients for resonant wave-particle interactions in a magnetized plasma. The method requires multiple inputs that can be obtained from observations - the plasma number density and ion composition, magnetic field strength, an estimate of wave intensity dependence on frequency and wavenormal angle, upper and lower frequency cut-offs, upper and lower cut-offs of wavenormal angle, the latitudinal extent of the waves and finally the wave intensity. As mentioned above, we will restrict our analysis in this paper to the variability of $D_{\alpha\alpha}$ in response to natural variability in just two of those inputs - the plasma frequency to gyrofreqeuncy ratio f_{pe}/f_{ce}, and the intensity of the waves. In this way we hope to show an illustration of the variability of the estimated diffusion coefficients when two of the input parameters are varied in a realistic way. The remaining inputs to the PADIE calculations are fixed as follows. We endeavour to use realistic values for the low-L region of the inner magnetosphere in this study, but note that simplifying choices have often been made to illustrate our point.

For the dependence of the hiss waves on frequency we fit a single Gaussian to the function given by (Li et al., 2015) for $L = 3$ to obtain an estimate of a reasonable plasmaspheric hiss spectra. The peak frequency of this spectrum is $f_{peak} = 252$ Hz, and the width $f_w = 194$ Hz. Note that this is a simplification of the function given by Li et al. (2015) for ease of use in the PADIE method, but is a reasonable estimate of the statistical hiss spectrum found therein. This information is then used to construct power spectral density

$$B^2(f) = \begin{cases} A^2 \exp\left(-\left(\frac{(f-f_{peak})}{f_w}\right)^2\right), & \text{for } f_{lc} \leq f \leq f_{uc} \\ 0, & \text{otherwise} \end{cases} \quad (1)$$

where A^2 is the peak wave spectral intensity, and $f_{lc} = 100$ Hz, $f_{uc} = 2$ kHz are the lower and upper frequency cut-offs respectively. Cut-off values are chosen in reference to previous work on diffusion caused by plasmaspheric hiss (e.g. Ni, Bortnik, Thorne, Ma, and Chen (2013); Ni et al. (2014); Meredith et al. (2009)). We experimented with a lower value for $f_{lc} = 20$ Hz, since Li et al. (2015) indicate that wave spectral intensity can extend well below 100Hz, especially on the dayside. However, changing the lower cut-off frequency made little difference to the values obtained here for $D_{\alpha\alpha}$, similar to results shown by Li et al. (2015). Peak wave spectral intensity A^2 is supplied by each observation of the wave spectral intensity at $f = 252$ Hz.

The wavenormal angle dependence of the plasmaspheric hiss is also simplified for this analysis. Near the geomagnetic equator, plasmaspheric hiss has been reported to propagate predominately parallel to the geomagnetic field, while at higher latitudes more oblique propagation is observed (Ni et al., 2014; Chen et al., 2012). In addition, Hartley et al. (2018) demonstrate that the distribution of wavenormal angles for plasmaspheric hiss is sometimes bimodal. We choose to use a Gaussian function in $\tan\phi$, where ϕ is the wavenormal angle, similarly to Ni et al. (2014). As mentioned above, we restrict our analysis to a small range of magnetic latitude, and so we use the wave normal angle distribution provided by Ni et al. (2014) for waves observed from $0-5^\circ$ magnetic latitude (i.e. $\phi_{lc} = 0^\circ$ and $\phi_{uc} = 20^\circ$). The wave normal angle distribution peak is set $\phi_{peak} = 0^\circ$, and the width $\phi_w = 15^\circ$. The wavevector magnitude $|k|$ is then calculated internally by PADIE using the magnetized cold plasma dispersion relation as discussed by Glauert and Horne (2005). An example of the refractive index $\mu = c|k|/\omega$ calculated during a single diffusion coefficient calculation, where c is the speed of light in a vacuum and $\omega = 2\pi f$, is shown in Figure S1 of the supplementary information.

The choices above motivate the latitudinal extent of waves used in the bounce-averaged calculations of PADIE, and so we restrict the latitudinal extent of the waves to $\lambda_{max} = 5^\circ$. Finally, the plasma composition is chosen and fixed to be an electron-proton plasma (i.e. in this analysis we ignore any heavier ion populations), and we restrict the number of resonances included in the calculations to the range $-10 < n < 10$. The relatively large number of resonances used in our calculation ensures that we capture the variability in $D_{\alpha\alpha}$ due to variability of input parameters, and not because we have inadvertently omitted small but important contributions from higher n resonances.

2.3 Measures of variability

The focus of this paper is to compare the variability in the input parameters for the diffusion coefficient calculation, and in the resulting diffusion coefficients themselves, so we choose the coefficient of variation c as our metric of variability. This standard statistical device is a normalized measure of the variability in different datasets. It is important to note that c takes different forms depending on the underlying distribution of the data. For normally-distributed data, the coefficient of variation is

$$c = \frac{\sigma}{\mu}, \quad (2)$$

where σ is the standard deviation of the data, and μ is the mean, and for log-normally distributed data

$$c = \sqrt{e^{\sigma_{ln}^2} - 1}, \quad (3)$$

Table 1: Number of observations used to estimate probability densities for each activity level.

L^*	$AE < 50$ nT	$50 < AE < 100$ nT	$100 < AE < 150$ nT	$AE > 150$ nT
2.5	800	381	239	150
3.0	1055	534	349	439
3.5	1387	695	801	389

where σ_{ln} is the standard deviation of the natural logarithm of the data. Of course, magnetospheric data are rarely normally, or log-normally distributed, but a visual inspection of the data in each volume bin indicates that they resemble one or other of those forms sufficiently that the coefficient of variation is a reasonable measure of the variability and a good way to compare the variability of parameters with different units. Hence we will use the above definitions of c as required. Interpretation of the values of c is relatively straightforward; if $c < 1$, then the data exhibits low variance, but if $c > 1$, then the data are highly variable.

3 Variability of observed input parameters

In all the analysis that follows, we present the variability of all the input data used to calculate the quasilinear diffusion coefficients, and analyze the variability for increasing geomagnetic activity. The temporal variability of diffusion coefficients is often captured using some measure of geomagnetic activity (e.g. Spasojevic et al. (2015); Meredith et al. (2018)). We use AE so that results may be compared with previous work (e.g. Meredith et al. (2018)). The activity bins used are $AE < 50$ nT, $50 < AE < 100$ nT, $100 < AE < 150$ nT, and $AE > 150$ nT. Because the occurrence of high values of activity is low, the highest activity bin includes a much wider range of activity than the other three. However, the ranges chosen should be sufficient to show any trends if they exist in the data. Table 1 shows the number of data points in each activity bin in our analysis. We have chosen to ensure that we have sufficient data coverage in each activity bin, rather than isolate the small number of very high values of geomagnetic activity. This compromise is necessary due to the small volume bins that we have chosen to minimize any variations due to radial locations. Future analyses may utilize larger volume bins as appropriate in order to get better resolution in geomagnetic activity parameter space.

Figure 2: (a-c) Normalized histograms showing probability density of magnetic field strength measurements in each of the three volumes studied. (d-f) Estimate of the probability density using a kernel density estimate for different ranges of AE (see legend)

The variability in magnetic field strength for all of the data in our study is indicated in Figure 2. The top row of the figure indicates a histogram of all the magnetic field strength data used in the study. The variability of magnetic field strength as a function of geomagnetic activity can be seen in the second row of Figure 2. Here we have used a kernel density estimate to provide an estimate of the probability distribution function for different values of activity. The solid black line indicates the lowest activity bin $AE <$ 50 nT, the dotted blue line indicates $50 < AE < 100$ nT, short dashed orange lines indicate $100 < AE < 150$ nT, and long dashed pink lines indicate $AE > 150$ nT. There

is not much variation in the distributions of magnetic field strength for increasing geomagnetic activity except at $L^* = 3.5$, where the highest range of AE corresponds to a slight shift in the probability density estimate towards lower values. As a "sanity check", we see that the average value of the magnetic field strength decreases with L^*.

For $L^* = 3.0$ and $L^* = 3.5$, the distribution appears fairly normal when inspected by eye. For $L^* = 2.5$, the distribution is more negatively skewed, yet the mean and standard deviation are still reasonable statistical measures of the distribution. As a result, we will use equation (2) to calculate the coefficient of variation for the magnetic field strength. We discover that $c \sim 0.04$ at all locations and for all values of geomagnetic activity studied here, which means that the standard deviation of the magnetic field strength measurements is less than 5% of the observed mean values.

Figure 3: (a-c) Normalized histograms showing probability density of number density estimates in each of the three volumes studied. (d-f) Estimate of the probability density using a kernel density estimate for different ranges of AE (see legend)

Figure 3 indicates the variability of number density, in the same format as Figure 2. As described in Section 2.1, the number density is estimated from the value of the upper hybrid frequency as detected by the Van Allen probe EMFISIS instrument. The data are unavoidably discretized due to the size of the finite frequency bins employed by EMFISIS. Nonetheless, the histogram and kernel density estimates of probability density give us a good indication of the underlying distribution of the measurements. A brief "sanity check" indicates that the mean observed number density decreases with L^*. The distributions do not have a simple form, but they appear normal enough that the mean and standard deviation are useful statistical characterizations of these data. Hence we use equation (2) to calculate the coefficient of variation for number density, and discover that the variability is larger than for the magnetic field strength, with $c = 0.31$ at $L^* = 2.5$, $c = 0.35$ at $L^* = 3.0$ and $c = 0.39$ at $L^* = 3.5$. As geomagnetic activity increases, there are no systematic changes in number density observations. At $L^* = 2.5$, the shape of the distribution changes markedly (but not systematically) with increasing geomagnetic activity, and the variability of decreases markedly for $50 < AE < 100$ nT. It is interesting that the overall range of measurements is largely unchanged with increasing activity levels. At $L^* = 3.0$, the measured number density exhibits very little change with increasing magnetic activity until the highest levels are reached. At high levels of activity, the variability dramatically decreases, while the mean remains similar. Finally, there is little change in the distribution of number density values at $L^* = 3.5$ with increasing activity until the highest levels are reached; then the distribution of number density observations is much more skewed towards lower values. In summary, for all L^*, there are no systematic changes in the distribution shape or range for number density at these selected locations.

Figure 4: (a-c) Normalized histograms showing probability density of f_{pe}/f_{ce} in each of the three volumes studied. (d-f) Estimate of the probability density using a kernel density estimate for different ranges of AE (see legend)

We combine co-located and simultaneous measurements of magnetic field strength and electron number density into the ratio f_{pe}/f_{ce} for use as an input to the PADIE calculations. The variability of this input parameter is shown in Figure 4 in the same for-

mat as for the magnetic field strength and number density analyses. The histograms indicate that the values of f_{pe}/f_{ce} at all locations studied are relatively normally distributed with well-defined means and standard deviations. The mean value of f_{pe}/f_{ce} increases with L^*. The variation of this parameter with increasing geomagnetic activity mirrors the patterns seen in Figure 3 for number density. Since f_{pe} varies with the square root of electron number density, the coefficient of variation for this PADIE input parameter is reduced from the variability seen for electron number density itself: $c = 0.16$ at $L^* = 2.5$, $c = 0.19$ at $L^* = 3.0$ and $c = 0.21$ at $L^* = 3.5$, all calculated using equation (2).

Figure 5: (a-c) Normalized histograms showing probability density of wave intensity at $f = 252$ Hz in each of the three volumes studied. (d-f) Estimate of the probability density using a kernel density estimate for different ranges of AE (see legend)

The second input for the PADIE calculations is the intensity of plasmaspheric hiss δB^2 at $f = 252$ Hz (see Section 2.2). Figure 5 shows the variability of this input parameter in the same format as above. In this instance, wave intensities are presented on a logarithmic scale, and the probability density estimates are calculated for $log_{10}(\delta B^2)$. The wave intensity data is presented in this form to highlight the logarithmic nature of the distribution, although it's important to note that the input parameter we use in the diffusion coefficient calculation in section 4 is δB^2 as required (Glauert & Horne, 2005). For all data (Figure 5a-c), the distribution of wave intensities does not have a simple form, but it is fair to say that they are highly non-Gaussian. At first glance, the distribution is closest to log-skew-normal with negative skew, and there is some evidence of multimodal structure at $L^* = 2.5$ and $L^* = 3.0$. We should note here that there are somewhere between 1500 and 2500 data points in each location bin. Given the size of the variability in this parameter, and the non-Gaussian nature of the distribution, it may be unwise to read too much into the details of the histograms.

Once we split the data by activity level, we observe that the strength of the waves tends to increase with geomagnetic activity. This is unsurprising, as the arithmetical average of the wave intensity in similar location bins increases with increasing activity (e.g. Meredith et al. (2004, 2018)). Note however that there is significant overlap between the probability density estimates. At $L^* = 3.0$ and $L^* = 3.5$ there does appear to be a thresholding effect during increasing geomagnetic activity, rather than a gradual increase in wave intensity as the geomagnetic activity increases. At both locations, the probability density estimates for $AE < 50$nT and $50 < AE < 100$nT are very similar, and the probability density estimates for $100 < AE < 150$nT and $AE > 150$nT are also very similar. Between the two lower activity levels and the two higher ones, there is a marked shift to the right in the distributions. Due to the logarithmic nature of the distributions, we use equation (3) to calculate the coefficient of variation here, with $c = 5.8$ at $L^* = 2.5$, $c = 9.7$ at $L^* = 3.0$, and $c = 5.8$ at $L^* = 3.5$. The amount of variance is much larger for the wave intensities than it is for the plasma or ambient magnetic field inputs.

Figure 6: One-dimensional probability functions of the wave intensity at $f = 252$ Hz as a function of f_{pe}/f_{ce}. The integral of each column in each panel is one. (a) $L^* = 2.5$ bin, (b) $L^* = 3.0$ bin and (c) $L^* = 3.5$ bin

It is important to discuss whether the two chosen inputs are independent. We construct a probability distribution function of the measured wave intensity at $f = 252$ Hz as a function of f_{pe}/f_{ce}. In Figure 6, every column in each of the three panels integrates to one (c.f. Figure 3 of Kellerman and Shprits (2012) and Figure 5 of Murphy et al. (2018)). There are no strong patterns in the dependence of wave intensity on frequency ratio at $L^* = 3.0$ or $L^* = 3.5$. There is a slight upwards trend for $L^* = 2.5$, although in all cases, the spread of measurements is large. The knowledge that the two inputs we propose to study in the calculation of diffusion coefficients are effectively independent will aid our interpretation of the results.

Recent investigations of hiss amplitude across a range of radial locations in the magnetosphere indicates that in some places, hiss amplitude varies more strongly with local number density than with radial location (Malaspina et al., 2018). For small L, these recent findings indicate that the variation of plasmaspheric hiss with number density is quite flat, and it is only at lower density (larger radial distance) that the variation becomes large. This echoes what we see in Figure 6 where there seems little dependence of wave amplitudes on the plasma frequency to gyrofrequency ratio. However, the results of Malaspina et al. (2018) indicate that input parameters for diffusion coefficient calculations may be interdependent in other parts of the inner magnetosphere.

4 Variability of $D_{\alpha\alpha}$

Figure 7: [top row] Normalized histograms showing probability density of $D_{\alpha\alpha}$ for $E = 0.5$ MeV and $\alpha = 30°$ in each of the three volumes studied. [bottom row] Estimate of the probability density using a kernel density estimate for different ranges of AE (see legend)

First, we study the variability of the pitch-angle diffusion coefficient $D_{\alpha\alpha}$ at a single energy and pitch-angle, $E = 0.5$ MeV and $\alpha = 30°$, chosen because $D_{\alpha\alpha}$ is shown to be strong at this energy and pitch-angle in previous analyses (e.g. Glauert et al. (2014a)). For each pair of co-located and contemporaneous observations of $\delta B^2(f = 252\text{Hz})$ and f_{pe}/f_{ce}, we calculate the value of $D_{\alpha\alpha}(E = 0.5\text{Mev}, \alpha = 30°)$. Figure 7 shows the variability of the resulting $D_{\alpha\alpha}$. The histograms of $D_{\alpha\alpha}$ are displayed on a logarithmic scale to demonstrate the nature of the variability. The median, upper and lower quartiles are also indicated with vertical lines. Like the distributions of δB, the distribution of $D_{\alpha\alpha}$ appears closest to a log-skew-normal with negative skew. The median is always less than the mode, which often coincides with the upper quartile. However, the variability changes dramatically between the three chosen location bins. At $L^* = 2.5$, the variability is very large, with a long tail of very small values. The variability is less at higher L^*, although the distributions do exhibit the same underlying log-skew-normal pattern. The distributions of $D_{\alpha\alpha}$ at $L^* = 3.0$ and $L^* = 3.5$ are very similar in shape, although the median is much higher at $L^* = 3.0$ than it is at $L^* = 3.5$.

Once we divide the distributions of $D_{\alpha\alpha}$ by activity level, there is no clear trend for the distributions at $L^* = 2.5$ with increasing geomagnetic activity. The distributions remain negatively skewed, but the median of the distribution is highest for the second highest activity level bin, and lowest for the second lowest activity level bin. At $L^* = 3.0$, the values of $D_{\alpha\alpha}$ are more ordered; $D_{\alpha\alpha}$ is likely to be higher as activity increases. At this location, the distribution is not skewed at the lowest activity level, becoming much more negatively skewed as the activity increases. At $L^* = 3.5$, the distributions of $D_{\alpha\alpha}$ are very similar for all three geomagnetic activity bins where $AE < 150$ nT. The low geomagnetic activity distributions are negatively skewed. For $AE > 150$ nT, the dis-

tribution is positively skewed and the median is much higher than for the other activity bins. Note that all the different distributions of $D_{\alpha\alpha}$ for different values of geomagnetic activity overlap considerably, and that the difference between their medians is small in comparison to their width. We will investigate this further in Section 5.

Figure 8: Coefficient of variation c for all input quantities and $D_{\alpha\alpha}$ for $E = 0.5$ MeV and $\alpha = 30°$. From top to bottom, c values for $D_{\alpha\alpha}$, δB^2, n_e, f_{pe}/f_{ce} and B_0. Stars indicate where c has been calculated using equation (2), and circles indicate where c has been calculated using equation (3).

The difference in variability between inputs to $D_{\alpha\alpha}$ and the diffusion coefficient itself is summarized in Figure 8. The stars indicate values of c calculated using equation 2 for normally-distributed variables, and circles indicate values of c calculated using equation 3 for log-normally distributed variables. The value of c for $D_{\alpha\alpha}$ at $L^* = 2.5$ is very large, and is not shown on the plot. It can be argued that equation 3 is an inappropriate description of variance when the underlying distribution is so skewed. The variability in all the inputs combines to yield an even larger variability in $D_{\alpha\alpha}$ at energy $E = 0.5$ MeV and $\alpha = 30°$. To understand the source of this variability at a single pitch-angle, we now consider $D_{\alpha\alpha}(\alpha)$.

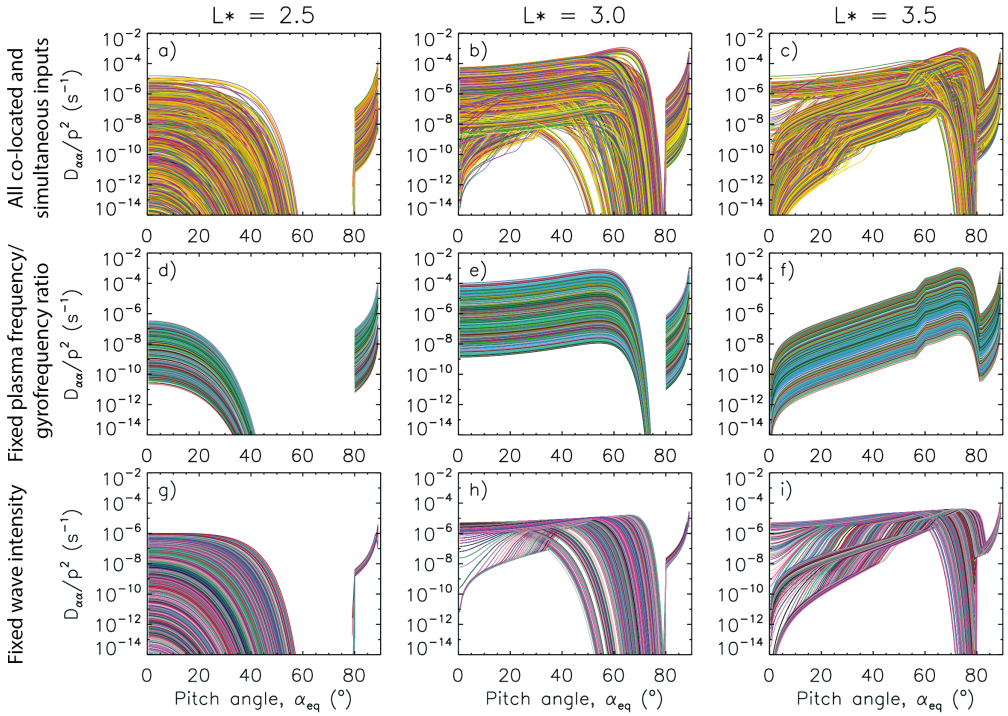

Figure 9: All the $D_{\alpha\alpha}(\alpha)$ for $E = 0.5$ MeV calculated in this study from co-located and simultaneous values of f_{pe}/f_{ce} and δB for (a) $L^* = 3.5$, (b) $L^* = 3.0$ and (c) $L^* = 2.5$. In (d-f), the plasma to gyrofrequency ratio is kept fixed at the average value, and the wave intensity is varied according to the observations. In (g-i), the wave intensity is fixed to the average value and the plasma to gyrofrequency ratio is varied according to the observations.

Figure 9(a-c) shows all the values of $D_{\alpha\alpha}$ calculated using PADIE from co-located and simultaneous observations of f_{pe}/f_{ce} and δB^2, this time demonstrating the dependence of $D_{\alpha\alpha}$ on α. It is clear that not only the value of $D_{\alpha\alpha}$ changes with the different inputs, but the functional form also varies. Horne et al. (2003b) demonstrate that the shape of $D_{\alpha\alpha}(\alpha)$ depends on the ratio of plasma frequency to gyrofrequency, and our results echo those earlier findings. The apparent independence of the two input parameters (see Figure 6) makes it feasible to investigate the variability of $D_{\alpha\alpha}$ when holding one of the inputs constant, to demonstrate the different ways in which the two input parameters influence the value of $D_{\alpha\alpha}$.

Figure 9(d-f) shows the variability in $D_{\alpha\alpha}$ when f_{pe}/f_{ce} is kept fixed at its mean observed value, and Figure 9(g-i) demonstrates the variability when δB^2 is kept at its mean observed value. Panels (d-f) emphasize that the intensity of the waves changes the size of $D_{\alpha\alpha}$ but not the shape. The variation in the wave intensity therefore affects electrons at all pitch angles equally, behaving like a scaling parameter on the rate of pitch angle diffusion. On the other hand, the number density and magnetic field strength significantly changes the shape and size of $D_{\alpha\alpha}$, as shown by panels (g-i) (note that in Figure 9, the vertical axes span many orders of magnitude). The observed variability in f_{pe}/f_{ce} can result in large changes in the range of resonant pitch-angles for the plasmaspheric hiss. For example, the range of cyclotron resonance at low pitch angles at $L^* = 2.5$ is significantly altered due to the observed variability in f_{pe}/f_{ce}. The range of variability of f_{pe}/f_{ce} likely explains the long negative tail of the distribution of $D_{\alpha\alpha}$ in Figure 7(a) as the resonant energies are controlled by the ratio. Hence variations in the plasma to gyrofrequency ratio alter the pitch angle range over which plasmaspheric hiss can scatter electrons via cyclotron resonances. As such, the pitch angle range that hiss waves can scatter into the loss cone is largely dependent on the value of f_{pe}/f_{ce}, particularly for the $L^* = 2.5$ and $L^* = 3.0$ bins. At $L^* = 2.5$, for some values of f_{pe}/f_{ce}, $D_{\alpha\alpha}$ can be less than 10^{-14} for all $\alpha < 80°$ suggesting that, under these conditions, hiss waves are not an effective loss mechanism for $E = 500$ keV electrons, regardless of the wave intensity. At the lowest range of pitch angles, the variability in the diffusion coefficients is maximized, which means that the potential loss of electrons into the loss-cone by pitch-angle scattering is also highly variable. At higher pitch angles ($> 80°$), where hiss waves scatter electrons via the Landau resonance, variations in f_{pe}/f_{ce} have little effect on the rate of scattering.

In addition to influencing the electron pitch angle range which can be lost from the radiation belt region due to scattering from plasmaspheric hiss, variations in the f_{pe}/f_{ce} ratio will affect electron pitch angle distributions. Cap-top pitch angle distributions (Zhao et al., 2018; Allison et al., 2018) are formed from hiss wave scattering due to the gap in $D_{\alpha\alpha}$ that arises between the cyclotron and Landau resonances (Lyons et al., 1972; Meredith et al., 2009). Figure 9g-i shows that variations in the plasma to gyrofrequency ratio alter the pitch angle range of this $D_{\alpha\alpha}$ gap and, as such, will influence the width of the resulting cap-top of pitch angle distributions. Note that panels d and e show minimal variation in the size of the $D_{\alpha\alpha}$ gap, indicating that varying δB power will have little influence on the form of cap top pitch angle distributions, but instead govern the rate at which this form is reached.

5 Discussion

Most empirical parameterized models of diffusion coefficients (e.g. Subbotin and Shprits (2009); Fok et al. (2011); Glauert et al. (2013); Horne et al. (2013); Tu et al. (2013)) use independent models of magnetic field and number density, and average values of observed wave parameters such as intensity along with an averaged functional dependence of intensity on frequency and wavenormal angle as inputs. In this work, we have instead investigated the range of possible diffusion coefficients obtained when using a large number of co-located and simultaneous measurements of input parameters. The two inputs

we have chosen for our demonstration do not have any obvious relationships (see Figure 6) and so it is reasonable to study the variability of $D_{\alpha\alpha}$ in response to each of the inputs independently.

Figure 10: A demonstration of the variability in $D_{\alpha\alpha}(E = 0.5\text{MeV}, \alpha = 30^\circ)$ for different methods of calculation: (i) values calculated using the method detailed in Section 7, (ii) a value calculated separately for the mean δB^2 and mean f_{pe}/f_{ce} in each location bin (asterisk), and a value calculated for the median δB^2 and median f_{pe}/f_{ce} (circle), (iii) values calculated using the mean f_{pe}/f_{ce} and all δB^2 values shown in Figure 5, (iv) values calculated using the mean δB^2, and all f_{pe}/f_{ce} values shown in Figure 4. For each of the cases (i), (iii) and (iv), the median is shown with a circle and upper/lower quartiles are indicated with the bar. Means are indicated with an asterisk.

The variability of $D_{\alpha\alpha}$ when calculated in different ways is summarized in Figure 10. For each location bin, we show the mean, median and interquartile range (IQR) when $D_{\alpha\alpha}$ is calculated using the full distribution of contemporaneous measurements (black), the full distribution of δB^2 and the mean value of f_{pe}/f_{ce} (red) and the full distribution of f_{pe}/f_{ce}, but the mean value of δB^2 (magenta). The value of $D_{\alpha\alpha}$ calculated using the mean values of f_{pe}/f_{ce} and δB^2 is shown with a blue asterisk, and the value of $D_{\alpha\alpha}$ calculated using the median values of f_{pe}/f_{ce} and δB^2 is shown with a blue circle. At all locations studied, the IQR is largest when the full variability of f_{pe}/f_{ce} and δB^2 is included. At $L^* = 2.5$, the plasma to gyrofrequency ratio is responsible for most of the variability, whereas at the other locations, the wave intensity variability plays a larger role. Interestingly, for $L^* = 3.5$, changing f_{pe}/f_{ce} leads to a small number of very large $D_{\alpha\alpha}$ values which skew the mean of the full sample (see the final column of the lowest panel in Figure 10).

While the median values of $D_{\alpha\alpha}$ do not seem very sensitive to the method of combining the measurements, the mean values of $D_{\alpha\alpha}$ are very sensitive. The underlying distributions of $D_{\alpha\alpha}$ shown in Figure 7 are log-skew-normal, and so the mean value of the distribution will be large for such large variances. Hence the mean value of $D_{\alpha\alpha}$ is largest for the calculation of $D_{\alpha\alpha}$ that yields the largest variance, i.e. when the variability of both inputs is incorporated. The median value, on the other hand, is affected much less by changes in the size of the variance of the distributions of $D_{\alpha\alpha}$. For all three L^* bins, the value of $D_{\alpha\alpha}$ calculated from the means of the input values is much less than the mean value of $D_{\alpha\alpha}$ calculated from all contemporaneous measurements (i.e. the asterisk in the first column of Figure 10 is always much larger than the asterisk in the second column). This suggests that using mean input values to calculate $D_{\alpha\alpha}$ does not capture the highest values of $D_{\alpha\alpha}$ at that location, and may indicate why event-specific diffusion coefficients (e.g. those used by Ripoll et al. (2016); Ma et al. (2018)) may yield quite different diffusion coefficients to the parameterized models. We note also that at $L^* = 2.5$, the variability of the ratio f_{pe}/f_{ce} appears to be responsible for most of the variability in $D_{\alpha\alpha}$ (see Figure 10), and yet the variability of f_{pe}/f_{ce} at $L^* = 2.5$ as measured by the coefficient of variation (Figure 8) is similar to that at all location bins studied in this analysis. The sensitivity of the diffusion coefficient to different input parameters also appears to vary from one location to another.

The results shown in the paper indicate that that effects of combining co-located and simultaneous measurements of the inputs for the diffusion coefficient calculation is to increase the variability of the resulting diffusion coefficients above the variability of the independent inputs (see Figure 10). Note that in this analysis, there is no obvious relationship between the variability, or underlying distribution, of the inputs, and the variability and underlying distribution of the diffusion coefficients, just that the variabil-

ity increases when the inputs are combined. The effects of variability in other inputs, such as wavenormal angle (Hartley et al., 2018), and wave frequency range (Li et al., 2015), should also be included in a future analysis. Indeed, the variability of plasma composition (Jahn et al., 2017) may also play a major role.

It is important to reiterate that the large values of variance in our diffusion coefficients result not just from the variability of the inputs (i.e. from the variability in plasma conditions and wave characteristics), but from the sensitivity of the calculation of the diffusion coefficients to those inputs. It is also important to note that the diffusion coefficients presented in this paper are for a single value of energy. When the plasma to gyrofrequency ratio is changed, the wave-particle resonance tends to move in energy-space; effectively, if diffusion is decreased at one energy due to changes in f_{pe}/f_{ce}, then it can be increased at another. Hence the variability in the diffusion coefficients at a single energy is not the full picture of phase space diffusion due to waves at a particular location, and the effects of the variability in $D_{\alpha\alpha}(E, \alpha)$ across all energies and pitch-angles should be investigated using numerical experiments. That is the natural next step for this work.

We do not yet know how the variability of diffusion coefficients presented here affects the modelling of diffusion processes in the outer radiation belt. The large values of variance in our diffusion coefficients indicate that a probabilistic model is worth pursuing to capture the physics of wave-particle interactions in the radiation belts. A stochastic parameterization is ideal to capture variable processes in physics-based models that incorporate empirical parameterization. The use of stochastic parameterizations in other branches of Earth Science (e.g. Berner et al. (2017); Pulido, Tandeo, Bocquet, Carrassi, and Lucini (2018)) demonstrates significant improvement over deterministic parameterizations for a range of different processes. The results presented in this paper provide the underlying distribution of the diffusion coefficients, and the size of the variance, for three different locations and provide some of the necessary information to test differences between deterministic and stochastic parameterization. A natural next step for this research is to perform the numerical experiments necessary to investigate whether descriptions that capture the variability of the diffusion coefficients provide different diffusion model evolution than their deterministic counterparts.

Until now, models of diffusion coefficients used in radiation belts models have incorporated temporal variability in drift- and bounce-averaged $D_{\alpha\alpha}$ by parameterizing the inputs for the diffusion coefficients (largely the wave parameters) by geomagnetic activity indices such as AE (e.g. Horne et al. (2013); Meredith et al. (2018)) or Kp (e.g. Albert et al. (2009); Ozeke et al. (2014); Glauert et al. (2018)). Here we discuss how well AE parameterizes the $D_{\alpha\alpha}$ by using a quantitative measure otherwise known as the separation proxy (Bentley et al., 2018b). There are a number of ways to describe the overlap between different bins of observations, but we will use this simple metric because the standard deviation of $\log(D_{\alpha\alpha})$ is relatively constant over all the geomagnetic activity bins shown in Figure 7(d-f). We use the signed ratio of the difference in mean values between adjacent geomagnetic activity bins to the standard deviation. Specifically, for two neighboring bins $b_i; b_{i+1}$, we define

$$\chi_S = \frac{(\mu_{i+1} - \mu_i)}{\frac{1}{2}(\sigma_i + \sigma_{i+1})} \tag{4}$$

where μ is the mean and σ_i the standard deviation of $\log(D_{\alpha\alpha})$. Note that in Bentley et al. (2018b), the quantity χ_S is unsigned, i.e. χ_S depends only on the absolute size of the difference between the means of neighboring bins. However, for our purposes, we note that a signed quantity retains valuable information, since an increase in geomagnetic activity does not necessarily guarantee an increase in the mean of $\log(D_{\alpha\alpha})$. The quantity χ_S is very similar to Cohen's d (Cohen, 1988), and much of the same interpretation can be used here (see Bentley et al. (2018b) for a discussion of why χ_S is preferable in

Table 2: Signed separation proxy χ_S for distributions of $D_{\alpha\alpha}$ for $E = 0.5$ MeV and $\alpha = 30°$ binned by geomagnetic activity in each location bin.

	$L^* = 2.5$	$L^* = 3.0$	$L^* = 3.5$
$AE < 50$ nT and $50 < AE < 100$ nT	-0.5	0.1	0.4
$50 < AE < 100$ nT and $100 < AE < 150$ nT	0.6	0.5	0.1
$100 < AE < 150$ nT and $AE > 150$ nT	-0.4	0.5	1.1

our case). When $\chi_S = 0$, the two distributions completely overlap, and when $\chi_S = 1$, the point of overlap between the two distributions is exactly one standard deviation from either mean, i.e. if both distributions were normal, then only 16% of data from each distribution would overlap when $\chi_S = 1$. Essentially, a larger value of χ_S indicates a "better" parameterization than a lower value, since highly overlapping distributions would indicate that our chosen parameter did not describe the diffusion coefficients well.

Table 2 shows the values of χ_S for the distributions of $log(D_{\alpha\alpha})$ shown in Figure 7(d-f). At $L^* = 2.5$, increasing geomagnetic activity does not correspond to an increase in the mean value of $log(D_{\alpha\alpha})$; the distributions jump around considerably as geomagnetic activity is increased. The expected increasing trends are seen at $L^* = 3.0$ and $L^* = 3.5$, with positive χ_S throughout, although there is significant overlap for some of the lower activity bins. We conclude that although increasing geomagnetic activity describes increasing values of $D_{\alpha\alpha}$ in some locations, this is not universal. An interesting feature of the distributions shown in Figure 7 is that for $L^* = 3.0$ and $L^* = 3.5$ there is evidence of a thresholding effect, rather than a steady increase in diffusion with geomagnetic activity. For $L^* = 3.0$, there is a large shift in the distribution towards the right between the $50 < AE < 100nT$ bin and the $100 < AE < 150nT$ bin. For $L^* = 3.5$, this large shift towards higher values of diffusion occurs between the $100 < AE < 150nT$ bin and the $1AE > 150nT$ bin. Of course, our small location bins have necessitated coarse-graining in geomagnetic activity space in order to preserve sufficient data to study the distributions of $D_{\alpha\alpha}$. Future analyses will consider larger volume bins (perhaps by including larger ranges in MLT or magnetic latitude) so that we have sufficient data coverage to study higher geomagnetic activity conditions in more detail and investigate the dependence of the diffusion coefficients on higher (and much rarer) values of geomagnetic activity.

6 Conclusions

In this study we determine the range of values of $D_{\alpha\alpha}$ due to plasmaspheric hiss as a result of realistic variations in two key input parameters. We chose three locations in the magnetic equatorial plane in the inner magnetosphere, all at $9 < \text{MLT} < 10$: $L^* = 2.5$, $L^* = 3.0$, and $L^* = 3.5$. The results from this study suggest that the diffusion coefficients calculated from co-located and simultaneous observations of plasma and wave properties exhibit large variability, and a highly non-Gaussian distribution. The input parameters to the diffusion coefficient calculation vary in different ways: the plasma frequency to gyrofrequency ratio is close to normally-distributed with a small variance, and the wave intensities are log-skew normally-distributed with a large variance. The extent of the variation in $D_{\alpha\alpha}$ varies in each of the three different locations we studied. As previous work suggests, variations in the wave intensity affects $D_{\alpha\alpha}$ at all pitch-angles, behaving like a scaling parameter for the diffusion coefficients. Variations in the plasma to gyrofrequency ratio change how effectively the plasmaspheric hiss interacts with electrons via cyclotron resonance and can radically alter the $D_{\alpha\alpha}(\alpha)$ profile at a constant

energy. For $L^* = 2.5$, the variations are largely due to changing plasma to gyrofrequency ratio, even though the variation in frequency ratio was very similar for the three locations studied. We conclude that the sensitivity of $D_{\alpha\alpha}$ can also be location-specific. For the $L^* = 3.0$ and $L^* = 3.5$ bins, the variations in $D_{\alpha\alpha}$ were primarily due to the wave intensity variations. However, for $L^* = 3.5$, changing frequency ratio leads to a small number of large $D_{\alpha\alpha}$ values which skews the mean of the full sample.

We suggest that it is important to capture the variability of the diffusion coefficients because these parameterizations are the key expression of sub-grid physics used in large-scale radiation belt diffusion models. We have seen that the variability of separate inputs combines to give increased variability in the calculated diffusion coefficients, not least because the quasilinear diffusion coefficients are not simple functions of the inputs. Note that we do not consider all sources of variability in this work, and that other important parameters, such as the variability of plasma composition and wave intensity as a function of frequency and wavenormal angle should also be investigated. The effect of the large variability in diffusion coefficients is currently unknown, and future work is planned to investigate the behaviour of diffusion models that include this variability. For example, knowledge of the variability of the diffusion coefficients can be used to great advantage in a stochastic parameterization of diffusion and this investigation is the first step towards a model that includes the full variability of wave-particle interactions possible in the radiation belts.

Acknowledgments

This research was supported by STFC grant ST/R000921/1, as well as the Natural Environment Research Council (NERC) Highlight Topic Grant NE/P01738X/1 (Rad-Sat BAS), NE/P017274/1 (Rad-Sat UoR), and NE/P017185/1 (Rad-Sat MSSL). HJA was supported by NERC Doctoral Training Programme NE/L002507/1 and RLT was supported by the Engineering and Physical Sciences Research Council (EPSRC) grant EP/L016613/1.

We acknowledge the NASA Van Allen Probes and Craig Kletzing for use of EMFISIS data. The EMFISIS data is available from https://emfisis.physics.uiowa.edu/data/index. Diffusion coefficient data displayed in this paper are available at http://dx.doi.org/10.17864/1947.212.

References

Agapitov, O., Artemyev, A., Krasnoselskikh, V., Khotyaintsev, Y. V., Mourenas, D., Breuillard, H., ... Rolland, G. (2013). Statistics of whistler mode waves in the outer radiation belt: Cluster staff-sa measurements. *Journal of Geophysical Research: Space Physics*, *118*(6), 3407-3420. doi: 10.1002/jgra.50312

Albert, J. M., Meredith, N. P., & Horne, R. B. (2009). Three-dimensional diffusion simulation of outer radiation belt electrons during the 9 October 1990 magnetic storm. *Journal of Geophysical Research: Space Physics*, *114*(A9). doi: 10.1029/2009JA014336

Albert, J. M., Starks, M. J., Horne, R. B., Meredith, N. P., & Glauert, S. A. (2016). Quasi-linear simulations of inner radiation belt electron pitch angle and energy distributions. *Geophysical Research Letters*, *43*(6), 2381-2388. doi: 10.1002/2016GL067938

Allison, H. J., Horne, R. B., Glauert, S. A., & Del Zanna, G. (2018). Determination of the equatorial electron differential flux from observations at low earth orbit. *Journal of Geophysical Research: Space Physics*. doi: 10.1029/2018ja025786

Bentley, S. N., Watt, C. E. J., Owens, M. J., & Rae, I. J. (2018a). Ulf wave activity in the magnetosphere: Resolving solar wind interdependencies to identify driving mechanisms. *Journal of Geophysical Research: Space Physics*, *123*(4), 2745-2771. doi: 10.1002/2017JA024740

Bentley, S. N., Watt, C. E. J., Rae, I. J., Owens, M. J., Murphy, K. R., Lockwood,

M., & Sandhu, J. K. (2018b). Capturing uncertainty in magnetospheric ultra-low frequency wave models. *Space Weather*, *under review*.

Berner, J., Achatz, U., Batt, L., Bengtsson, L., Cmara, A. d. l., Christensen, H. M., ... Yano, J.-I. (2017). Stochastic parameterization: Toward a new view of weather and climate models. *Bulletin of the American Meteorological Society*, *98*(3), 565-588. doi: 10.1175/BAMS-D-15-00268.1

Blum, L. W., Halford, A., Millan, R., Bonnell, J. W., Goldstein, J., Usanova, M., ... Li, X. (2015). Observations of coincident EMIC wave activity and duskside energetic electron precipitation on 1819 January 2013. *Geophysical Research Letters*, *42*(14), 5727-5735. doi: 10.1002/2015GL065245

Chen, L., Li, W., Bortnik, J., & Thorne, R. M. (2012). Amplification of whistler-mode hiss inside the plasmasphere. *Geophysical Research Letters*, *39*(8). doi: 10.1029/2012GL051488

Cohen, J. (1988). *Statistical power analysis for the behavioral sciences*. Lawrence Erlbaum Associates.

Drozdov, A. Y., Shprits, Y. Y., Usanova, M. E., Aseev, N. A., Kellerman, A. C., & Zhu, H. (2017). EMIC wave parameterization in the long-term VERB code simulation. *Journal of Geophysical Research: Space Physics*, *122*(8), 8488-8501. doi: 10.1002/2017JA024389

Fei, Y., Chan, A. A., Elkington, S. R., & Wiltberger, M. J. (2006). Radial diffusion and mhd particle simulations of relativistic electron transport by ulf waves in the september 1998 storm. *Journal of Geophysical Research: Space Physics*, *111*(A12). doi: 10.1029/2005JA011211

Fok, M.-C., Glocer, A., Zheng, Q., Horne, R., Meredith, N., Albert, J., & Nagai, T. (2011). Recent developments in the radiation belt environment model. *Journal of Atmospheric and Solar-Terrestrial Physics*, *73*(11), 1435 – 1443. doi: 10.1016/j.jastp.2010.09.033

Glauert, S. A., & Horne, R. B. (2005). Calculation of pitch angle and energy diffusion coefficients with the padie code. *Journal of Geophysical Research: Space Physics*, *110*(A4). doi: 10.1029/2004JA010851

Glauert, S. A., Horne, R. B., & Meredith, N. P. (2013). Three-dimensional electron radiation belt simulations using the BAS Radiation Belt Model with new diffusion models for chorus, plasmaspheric hiss, and lightning-generated whistlers. *Journal of Geophysical Research: Space Physics*, *119*(1), 268-289. doi: 10.1002/2013JA019281

Glauert, S. A., Horne, R. B., & Meredith, N. P. (2014a). Three-dimensional electron radiation belt simulations using the BAS Radiation Belt Model with new diffusion models for chorus, plasmaspheric hiss, and lightning-generated whistlers. *Journal of Geophysical Research: Space Physics*, *119*(1), 268-289. doi: 10.1002/2013JA019281

Glauert, S. A., Horne, R. B., & Meredith, N. P. (2018). A 30-year simulation of the outer electron radiation belt. *Space Weather*, *0*(0). doi: 10.1029/2018SW001981

Hartley, D. P., Kletzing, C. A., Santolk, O., Chen, L., & Horne, R. B. (2018). Statistical properties of plasmaspheric hiss from van allen probes observations. *Journal of Geophysical Research: Space Physics*, *123*(4), 2605-2619. doi: 10.1002/2017JA024593

Horne, R. B., Glauert, S. A., & Thorne, R. M. (2003b). Resonant diffusion of radiation belt electrons by whistler-mode chorus. *Geophysical Research Letters*, *30*, 1493–1496.

Horne, R. B., Kersten, T., Glauert, S. A., Meredith, N. P., Boscher, D., Sicard-Piet, A., ... Li, W. (2013). A new diffusion matrix for whistler mode chorus waves. *Journal of Geophysical Research: Space Physics*, *118*(10), 6302-6318. doi: 10.1002/jgra.50594

Horne, R. B., Meredith, N. M., Glauert, S. A., & Kersten, T. (2016). Wave driven

diffusion in radiation belt dynamics. In G. Balasis, I. A. Daglis, & I. R. Mann (Eds.), *Waves, particles, and storms in geospace: a complex interplay* (p. 217-243). Oxford: Oxford University Press.

Horne, R. B., Thorne, R. M., Glauert, S. A., Albert, J. M., Meredith, N. P., & Anderson, R. R. (2005a). Timescale for radiation belt electron acceleration by whistler mode chorus waves. *Journal of Geophysical Research: Space Physics*, *110*(A3). doi: 10.1029/2004JA010811

Horne, R. B., Thorne, R. M., Shprits, Y. Y., Meredith, N. M., Glauert, S. A., Smith, A. J., ... Decreau, P. M. E. (2005b). Wave acceleration of electrons in the Van Allen radiation belts. *Nature*, *437*. doi: 10.1038/nature03939

Jahn, J.-M., Goldstein, J., Reeves, G. D., Fernandes, P. A., Skoug, R. M., Larsen, B. A., & Spence, H. E. (2017). The warm plasma composition in the inner magnetosphere during 20122015. *Journal of Geophysical Research: Space Physics*, *122*(11), 11,018-11,043. doi: 10.1002/2017JA024183

Kellerman, A. C., & Shprits, Y. Y. (2012). On the influence of solar wind conditions on the outer-electron radiation belt. *Journal of Geophysical Research: Space Physics*, *117*(A5). doi: 10.1029/2011JA017253

Kersten, T., Horne, R. B., Glauert, S. A., Meredith, N. P., Fraser, B. J., & Grew, R. S. (2014). Electron losses from the radiation belts caused by EMIC waves. *Journal of Geophysical Research: Space Physics*, *119*(11), 8820-8837. doi: 10.1002/2014JA020366

Kim, K.-C., Shprits, Y., Subbotin, D., & Ni, B. (2011). Understanding the dynamic evolution of the relativistic electron slot region including radial and pitch angle diffusion. *Journal of Geophysical Research: Space Physics*, *116*(A10).

Kletzing, C. A., Kurth, W. S., Acuna, M., MacDowall, R. J., Torbert, R. B., Averkamp, T., ... Tyler, J. (2013, Nov 01). The electric and magnetic field instrument suite and integrated science (emfisis) on rbsp. *Space Science Reviews*, *179*(1), 127–181. Retrieved from `https://doi.org/10.1007/s11214-013-9993-6` doi: 10.1007/s11214-013-9993-6

Koons, H. C., & Roeder, J. L. (1990, October). A survey of equatorial magnetospheric wave activity between 5 and 8 R_E. *Planetary and Space Science*, *38*, 1335-1341. doi: 10.1016/0032-0633(90)90136-E

Kurth, W. S., De Pascuale, S., Faden, J. B., Kletzing, C. A., Hospodarsky, G. B., Thaller, S., & Wygant, J. R. (2015). Electron densities inferred from plasma wave spectra obtained by the waves instrument on van allen probes. *Journal of Geophysical Research: Space Physics*, *120*(2), 904-914. doi: 10.1002/2014JA020857

Lam, M. M., Horne, R. B., Meredith, N. P., & Glauert, S. A. (2007). Modeling the effects of radial diffusion and plasmaspheric hiss on outer radiation belt electrons. *Geophysical Research Letters*, *34*(20). doi: 10.1029/2007GL031598

Lejosne, S., Boscher, D., Maget, V., & Rolland, G. (2012). Bounce-averaged approach to radial diffusion modeling: From a new derivation of the instantaneous rate of change of the third adiabatic invariant to the characterization of the radial diffusion process. *Journal of Geophysical Research: Space Physics*, *117*(A8). doi: 10.1029/2012JA018011

Li, W., Ma, Q., Thorne, R. M., Bortnik, J., Kletzing, C. A., Kurth, W. S., ... Nishimura, Y. (2015). Statistical properties of plasmaspheric hiss derived from Van Allen Probes data and their effects on radiation belt electron dynamics. *Journal of Geophysical Research: Space Physics*, *120*(5), 3393-3405. doi: 10.1002/2015JA021048

Li, W., Thorne, R. M., Bortnik, J., Tao, X., & Angelopoulos, V. (2012). Characteristics of hiss-like and discrete whistler-mode emissions. *Geophysical Research Letters*, *39*(18). doi: 10.1029/2012GL053206

Lyons, L. R., Thorne, R. M., & Kennel, C. F. (1972). Pitch-angle diffusion of radiation belt electrons within the plasmasphere. *Journal of Geophysical Research*,

77(19), 3455-3474. doi: 10.1029/JA077i019p03455

Ma, Q., Li, W., Bortnik, J., Thorne, R. M., Chu, X., Ozeke, L. G., ... Claudepierre, S. G. (2018). Quantitative evaluation of radial diffusion and local acceleration processes during gem challenge events. *Journal of Geophysical Research: Space Physics*, *123*(3), 1938-1952. doi: 10.1002/2017JA025114

Ma, Q., Li, W., Thorne, R. M., Ni, B., Kletzing, C. A., Kurth, W. S., ... Angelopoulos, V. (2015). Modeling inward diffusion and slow decay of energetic electrons in the earth's outer radiation belt. *Geophysical Research Letters*, *42*(4), 987-995. doi: 10.1002/2014GL062977

Malaspina, D. M., Jaynes, A. N., Hospodarsky, G., Bortnik, J., Ergun, R. E., & Wygant, J. (2017). Statistical properties of low-frequency plasmaspheric hiss. *Journal of Geophysical Research: Space Physics*, *122*(8), 8340-8352. doi: 10.1002/2017JA024328

Malaspina, D. M., Ripoll, J.-F., Chu, X., Hospodarsky, G., & Wygant, J. (2018). Variation in plasmaspheric hiss wave power with plasma density. *Geophysical Research Letters*, *45*(18), 9417-9426. doi: 10.1029/2018GL078564

Mann, I. R., Ozeke, L. G., Murphy, K. R., Claudepierre, S. G., Turner, D. L., Baker, D. N., ... Honary, F. (2016). Explaining the dynamics of the ultra-relativistic third Van Allen radiation belt. *Nature Physics*, *12*, 978-983.

Meredith, N. P., Horne, R. B., & Anderson, R. R. (2001). Substorm dependence of chorus amplitudes: Implications for the acceleration of electrons to relativistic energies. *Journal of Geophysical Research: Space Physics*, *106*(A7), 13165-13178. doi: 10.1029/2000JA900156

Meredith, N. P., Horne, R. B., Glauert, S. A., & Anderson, R. R. (2007). Slot region electron loss timescales due to plasmaspheric hiss and lightning-generated whistlers. *Journal of Geophysical Research: Space Physics*, *112*(A8). doi: 10.1029/2007JA012413

Meredith, N. P., Horne, R. B., Glauert, S. A., Baker, D. N., Kanekal, S. G., & Albert, J. M. (2009). Relativistic electron loss timescales in the slot region. *Journal of Geophysical Research: Space Physics*, *114*(A3). doi: 10.1029/2008JA013889

Meredith, N. P., Horne, R. B., Glauert, S. A., Thorne, R. M., Summers, D., Albert, J. M., & Anderson, R. R. (2006). Energetic outer zone electron loss timescales during low geomagnetic activity. *Journal of Geophysical Research: Space Physics*, *111*(A05212). doi: 10.1029/2005JA011516

Meredith, N. P., Horne, R. B., Kersten, T., Li, W., Bortnik, J., Sicard, A., & Yearby, K. H. (2018). Global model of plasmaspheric hiss from multiple satellite observations. *Journal of Geophysical Research: Space Physics*, *123*(6), 4526-4541. doi: 10.1029/2018JA025226

Meredith, N. P., Horne, R. B., Thorne, R. M., Summers, D., & Anderson, R. R. (2004). Substorm dependence of plasmaspheric hiss. *Journal of Geophysical Research: Space Physics*, *109*(A6). doi: 10.1029/2004JA010387

Miyoshi, Y. S., Jordanova, V. K., Morioka, A., & Evans, D. S. (2005). Solar cycle variations of the electron radiation belts: Observations and radial diffusion simulation. *Space Weather*, *2*(10). doi: 10.1029/2004SW000070

Murphy, K. R., Inglis, A. R., Sibeck, D. G., Rae, I. J., Watt, C. E. J., Silveira, M., ... Nakamura, R. (2018). Determining the mode, frequency, and azimuthal wave number of ULF waves during a HSS and moderate geomagnetic storm. *Journal of Geophysical Research: Space Physics*, *123*(8), 6457-6477. doi: 10.1029/2017JA024877

Ni, B., Bortnik, J., Thorne, R. M., Ma, Q., & Chen, L. (2013). Resonant scattering and resultant pitch angle evolution of relativistic electrons by plasmaspheric hiss. *Journal of Geophysical Research: Space Physics*, *118*(12), 7740-7751. doi: 10.1002/2013JA019260

Ni, B., Li, W., Thorne, R. M., Bortnik, J., Ma, Q., Chen, L., ... Claudepierre,

S. G. (2014). Resonant scattering of energetic electrons by unusual low-frequency hiss. *Geophysical Research Letters*, *41*(6), 1854-1861. doi: 10.1002/2014GL059389

Ni, B., Thorne, R. M., Shprits, Y. Y., & Bortnik, J. (2008). Resonant scattering of plasma sheet electrons by whistler-mode chorus: Contribution to diffuse auroral precipitation. *Geophysical Research Letters*, *35*(11). doi: 10.1029/2008GL034032

Olson, W. P., & Pfizer, K. (1977). *Magnetospheric magnetic field modelling annual scientific report* (Tech. Rep. No. AFOSR Contract No. F44620-75-c-0033).

Ozeke, L. G., Mann, I. R., Murphy, K. R., Rae, I. J., & Milling, D. K. (2014). Analytic expressions for ULF wave radiation belt radial diffusion coefficients. *Journal of Geophysical Research: Space Physics*, *119*(3), 1587-1605. doi: 10.1002/2013JA019204

Pulido, M., Tandeo, P., Bocquet, M., Carrassi, A., & Lucini, M. (2018). Stochastic parameterization identification using ensemble kalman filtering combined with maximum likelihood methods. *Tellus A: Dynamic Meteorology and Oceanography*, *70*(1), 1442099. doi: 10.1080/16000870.2018.1442099

Reeves, G. D., Chen, Y., Cunningham, G. S., Friedel, R. W. H., Henderson, M. G., Jordanova, V. K., ... Zaharia, S. (2012). Dynamic Radiation Environment Assimilation Model: DREAM. *Space Weather*, *10*(3). doi: 10.1029/2011SW000729

Ripoll, J.-F., Reeves, G. D., Cunningham, G. S., Loridan, V., Denton, M., Santolk, O., ... Ukhorskiy, A. Y. (2016). Reproducing the observed energy-dependent structure of Earth's electron radiation belts during storm recovery with an event-specific diffusion model. *Geophysical Research Letters*, *43*(11), 5616-5625. doi: 10.1002/2016GL068869

Ripoll, J.-F., Santolk, O., Reeves, G. D., Kurth, W. S., Denton, M. H., Loridan, V., ... Turner, D. L. (2017). Effects of whistler mode hiss waves in March 2013. *Journal of Geophysical Research: Space Physics*, *122*(7), 7433-7462. doi: 10.1002/2017JA024139

Russell, C. T., Holzer, R. E., & Smith, E. J. (1970). Ogo 3 observations of elf noise in the magnetosphere: 2. the nature of the equatorial noise. *Journal of Geophysical Research*, *75*(4), 755-768. doi: 10.1029/JA075i004p00755

Santolík, O., Němec, F., Gereová, K., Macúšová, E., de Conchy, Y., & Cornilleau-Wehrlin, N. (2004). Systematic analysis of equatorial noise below the lower hybrid frequency. *Annales Geophysicae*, *22*(7), 2587–2595. Retrieved from `https://www.ann-geophys.net/22/2587/2004/` doi: 10.5194/angeo-22-2587-2004

Santolk, O., & Gurnett, D. A. (2003a). Transverse dimensions of chorus in the source region. *Geophysical Research Letters*, *30*(2). doi: 10.1029/2002GL016178

Santolk, O., Gurnett, D. A., Pickett, J. S., Parrot, M., & Cornilleau-Wehrlin, N. (2003b). Spatio-temporal structure of storm-time chorus. *Journal of Geophysical Research: Space Physics*, *108*(A7). doi: 10.1029/2002JA009791

Sheeley, B. W., Moldwin, M. B., Rassoul, H. K., & Anderson, R. R. (2001). An empirical plasmasphere and trough density model: Crres observations. *Journal of Geophysical Research: Space Physics*, *106*(A11), 25631-25641. doi: 10.1029/2000JA000286

Spasojevic, M., Shprits, Y. Y., & Orlova, K. (2015). Global empirical models of plasmaspheric hiss using Van Allen Probes. *Journal of Geophysical Research: Space Physics*, *120*(12), 10,370-10,383. doi: 10.1002/2015JA021803

Subbotin, D. A., & Shprits, Y. Y. (2009). Three-dimensional modeling of the radiation belts using the Versatile Electron Radiation Belt (VERB) code. *Space Weather*, *7*(10). doi: 10.1029/2008SW000452

Summers, D., Ni, B., Meredith, N. P., Horne, R. B., Thorne, R. M., Moldwin, M. B.,

& Anderson, R. R. (2008). Electron scattering by whistler-mode elf hiss in plasmaspheric plumes. *Journal of Geophysical Research: Space Physics*, *113*(A4). doi: 10.1029/2007JA012678

Thompson, R. L., Watt, C. E. J., & Williams, P. D. (2018). Exploring the impacts of variability in the radial diffusion problem. *Journal of Geophysical Research: Space Physics*, *under review*.

Thorne, R. M. (2010). Radiation belt dynamics: The importance of wave-particle interactions. *Geophysical Research Letters*, *37*(22). doi: 10.1029/2010GL044990

Thorne, R. M., Smith, E. J., Burton, R. K., & Holzer, R. E. (1973). Plasmaspheric hiss. *Journal of Geophysical Research*, *78*(10), 1581-1596. doi: 10.1029/JA078i010p01581

Tsurutani, B. T., & Smith, E. J. (1977). Two types of magnetospheric ELF chorus and their substorm dependences. *Journal of Geophysical Research*, *82*(32), 5112-5128. Retrieved from `https://agupubs.onlinelibrary.wiley.com/doi/abs/10.1029/JA082i032p05112` doi: 10.1029/JA082i032p05112

Tu, W., Cunningham, G. S., Chen, Y., Henderson, M. G., Camporeale, E., & Reeves, G. D. (2013). Modeling radiation belt electron dynamics during gem challenge intervals with the dream3d diffusion model. *Journal of Geophysical Research: Space Physics*, *118*(10), 6197-6211. doi: 10.1002/jgra.50560

Tu, W., Cunningham, G. S., Chen, Y., Morley, S. K., Reeves, G. D., Blake, J. B., ... Spence, H. (2014). Event-specific chorus wave and electron seed population models in dream3d using the van allen probes. *Geophysical Research Letters*, *41*(5), 1359-1366. doi: 10.1002/2013GL058819

Varotsou, A., Boscher, D., Bourdarie, S., Horne, R. B., Glauert, S. A., & Meredith, N. P. (2008). Simulation of the outer radiation belt electrons near geosynchronous orbit including both radial diffusion and resonant interaction with whistler-mode chorus waves. *Geophysical Research Letters*, *32*(19). doi: 10.1029/2005GL023282

Watt, C. E. J., Rae, I. J., Murphy, K. R., Anekallu, C., Bentley, S. N., & Forsyth, C. (2017). The parameterization of wave-particle interactions in the Outer Radiation Belt. *Journal of Geophysical Research: Space Physics*, *122*(9), 9545-9551. doi: 10.1002/2017JA024339

Zhao, H., Friedel, R. H. W., Chen, Y., Reeves, G. D., Baker, D. N., Li, X., ... Spence, H. E. (2018). An empirical model of radiation belt electron pitch angle distributions based on van allen probes measurements. *Journal of Geophysical Research: Space Physics*, *123*(5), 3493-3511. doi: 10.1029/2018JA025277

Figure 1.

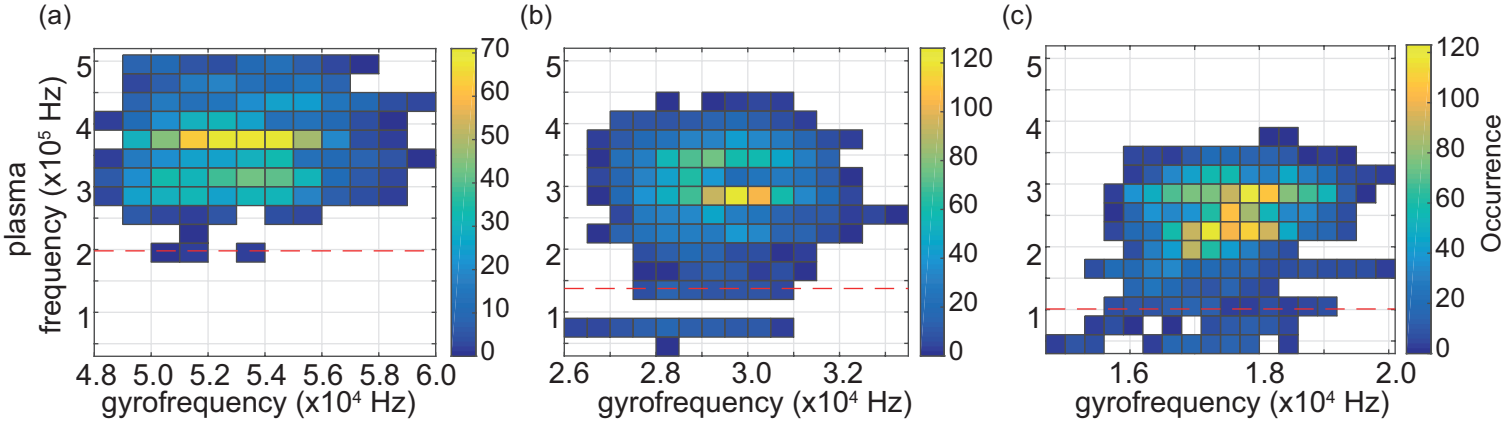
(a)
(b)
(c)
plasma frequency (x10^5 Hz)
gyrofrequency (x10^4 Hz)
gyrofrequency (x10^4 Hz)
gyrofrequency (x10^4 Hz)
Occurrence
1
2
3
4
5
4.8 5.0 5.2 5.4 5.6 5.8 6.0
2.6 2.8 3.0 3.2
1.6 1.8 2.0
0 10 20 30 40 50 60 70
0 20 40 60 80 100 120
0 20 40 60 80 100 120

Figure 2.

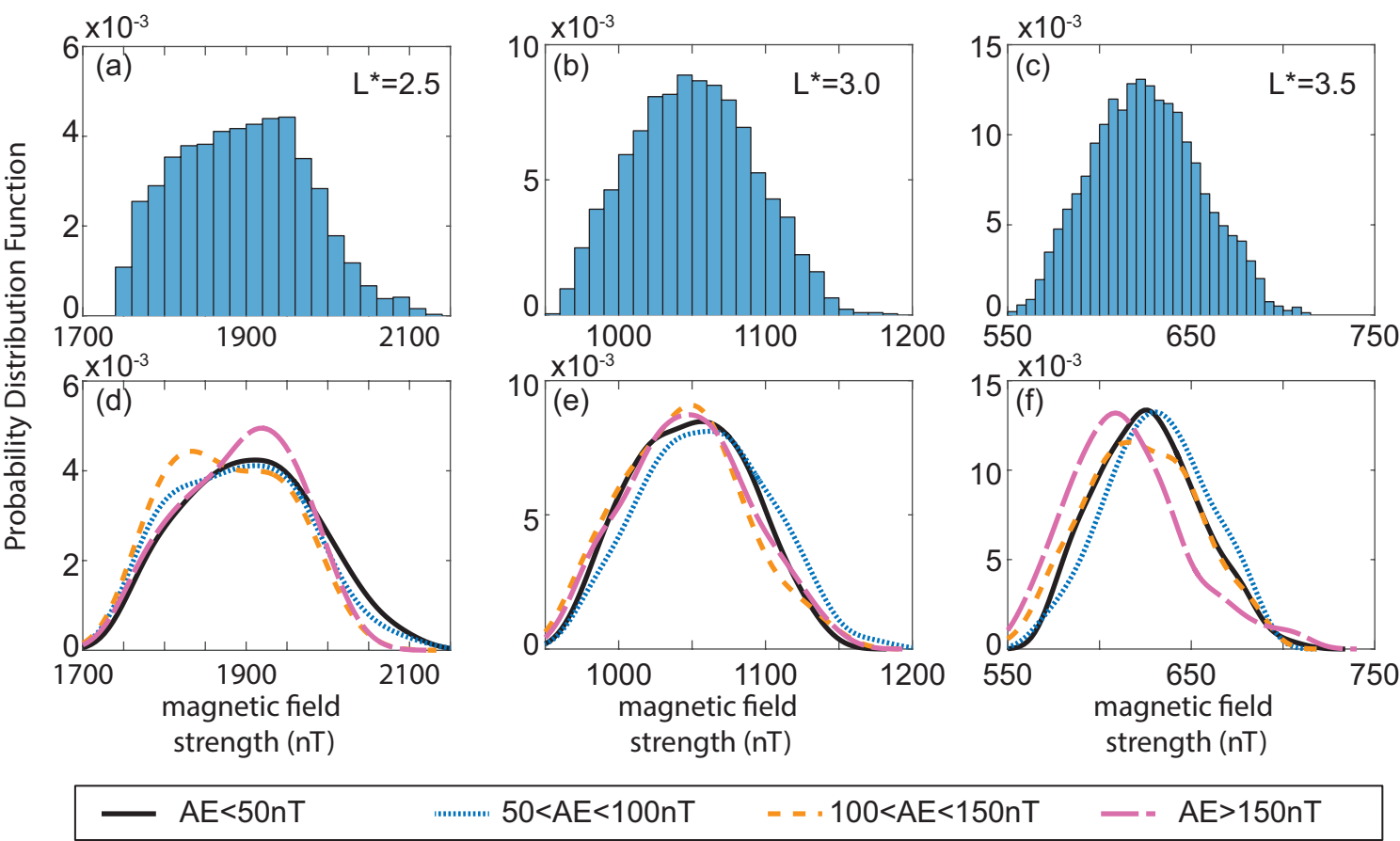
Probability Distribution Function
x10-3
(a)
L*=2.5
(b)
L*=3.0
(c)
L*=3.5
(d)
(e)
(f)
magnetic field strength (nT)
AE<50nT
50<AE<100nT
100<AE<150nT
AE>150nT

Figure 3.

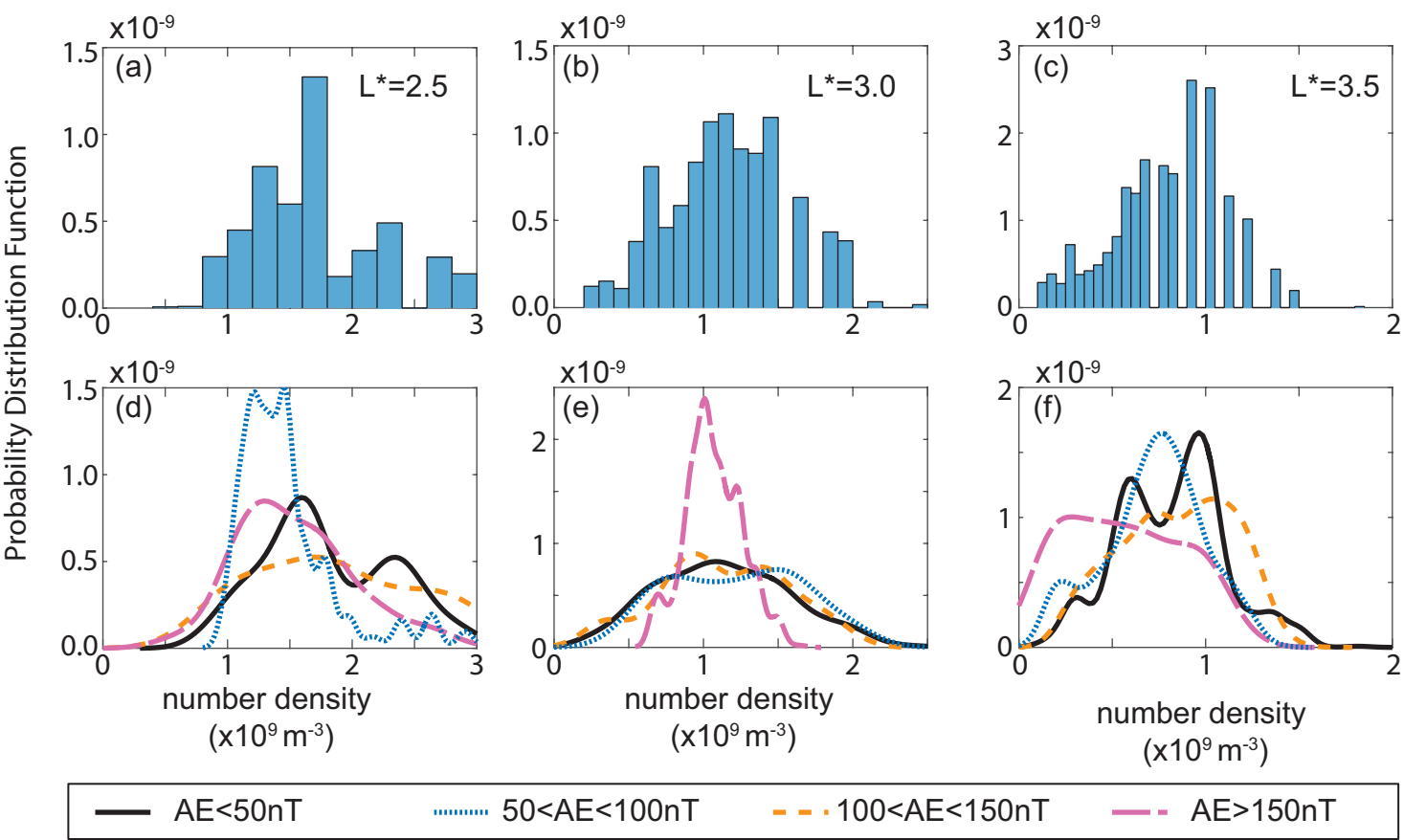
Probability Distribution Function
x10-9
(a)
L*=2.5
(b)
L*=3.0
(c)
L*=3.5
(d)
(e)
(f)
number density
(x10⁹ m⁻³)
AE<50nT
50<AE<100nT
100<AE<150nT
AE>150nT

Figure 4.

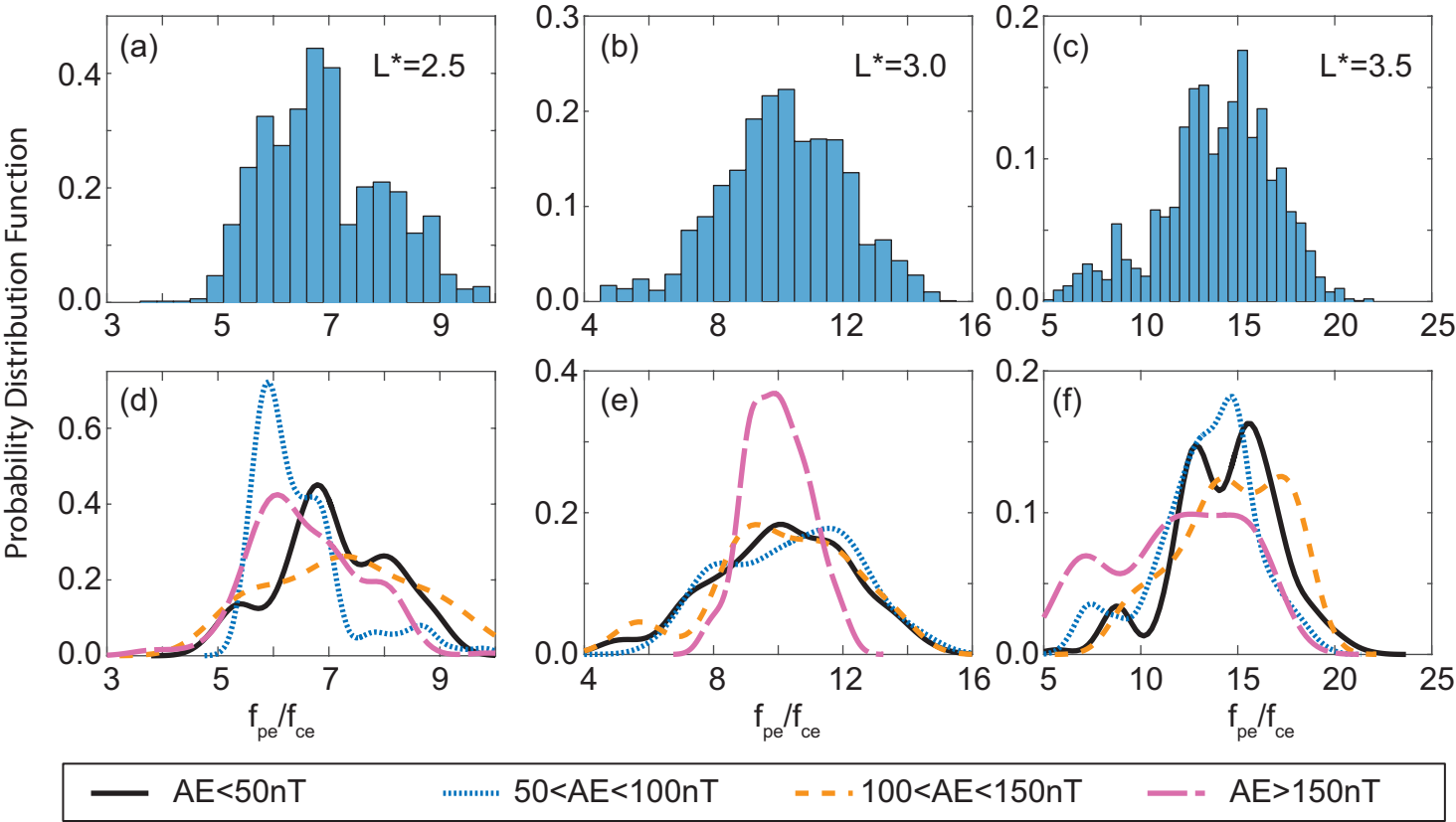
(a)
L*=2.5
(b)
L*=3.0
(c)
L*=3.5
(d)
(e)
(f)
Probability Distribution Function
f_pe/f_ce
f_pe/f_ce
f_pe/f_ce
AE<50nT
50<AE<100nT
100<AE<150nT
AE>150nT

Figure 5.

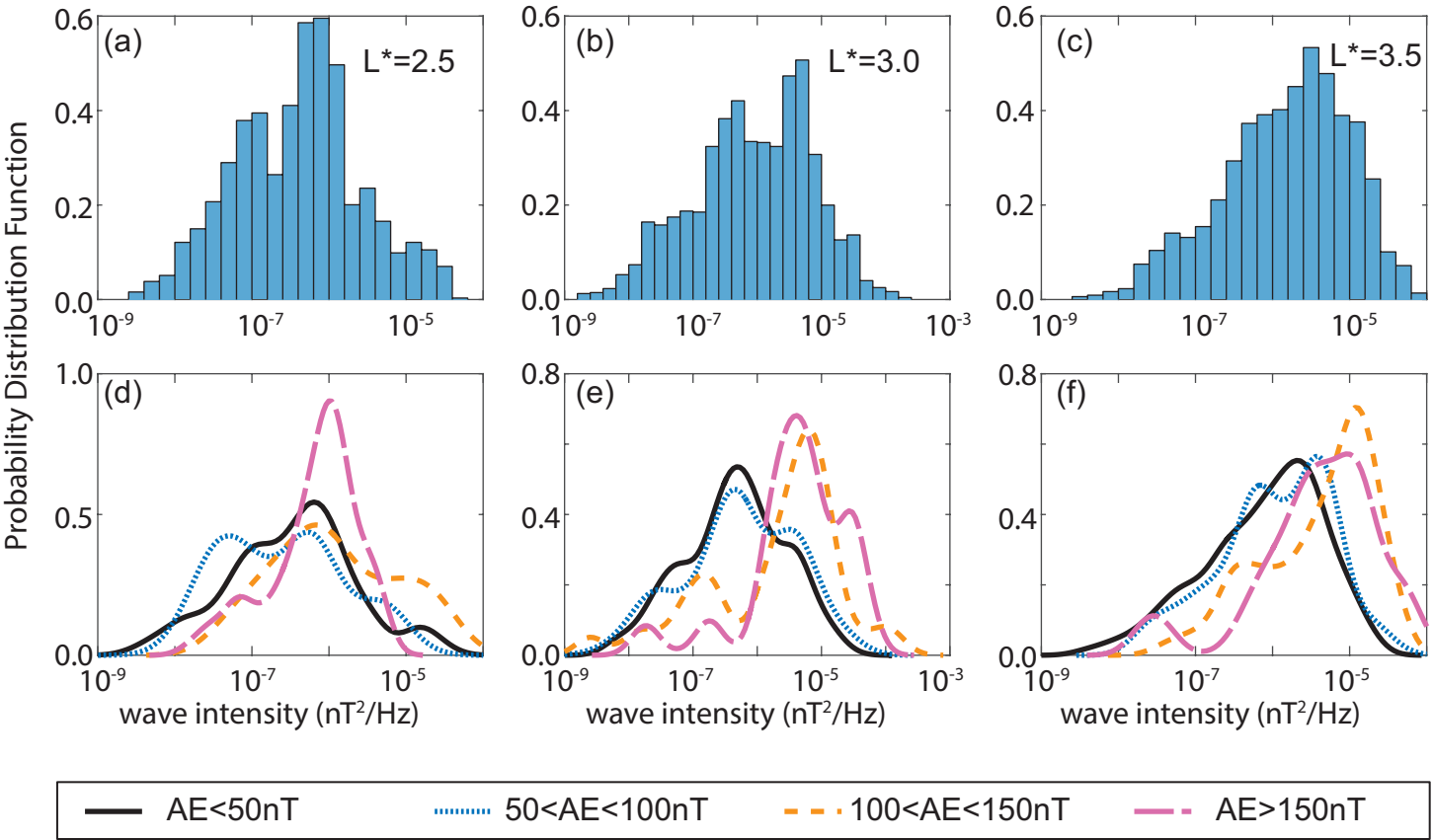
(a)
L*=2.5
(b)
L*=3.0
(c)
L*=3.5
(d)
(e)
(f)
Probability Distribution Function
wave intensity (nT²/Hz)
wave intensity (nT²/Hz)
wave intensity (nT²/Hz)
AE<50nT
50<AE<100nT
100<AE<150nT
AE>150nT

Figure 6.

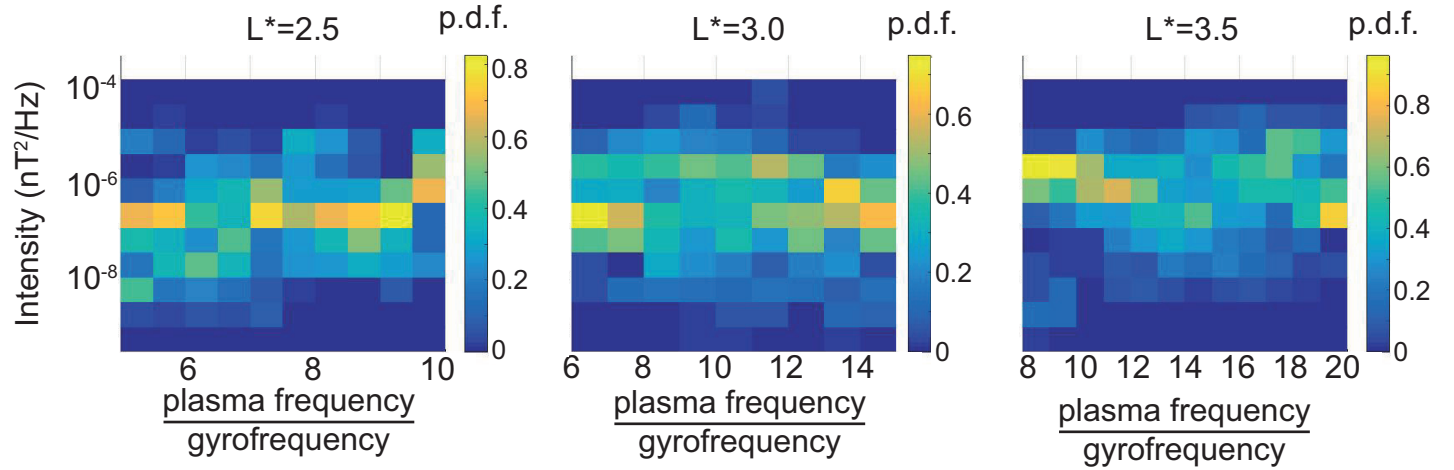
L*=2.5
p.d.f.
0.8
0.6
0.4
0.2
0
Intensity (nT²/Hz)
10⁻⁴
10⁻⁶
10⁻⁸
6
8
10
plasma frequency
gyrofrequency
L*=3.0
p.d.f.
0.6
0.4
0.2
0
6
8
10
12
14
plasma frequency
gyrofrequency
L*=3.5
p.d.f.
0.8
0.6
0.4
0.2
0
8
10
12
14
16
18
20
plasma frequency
gyrofrequency

Figure 7.

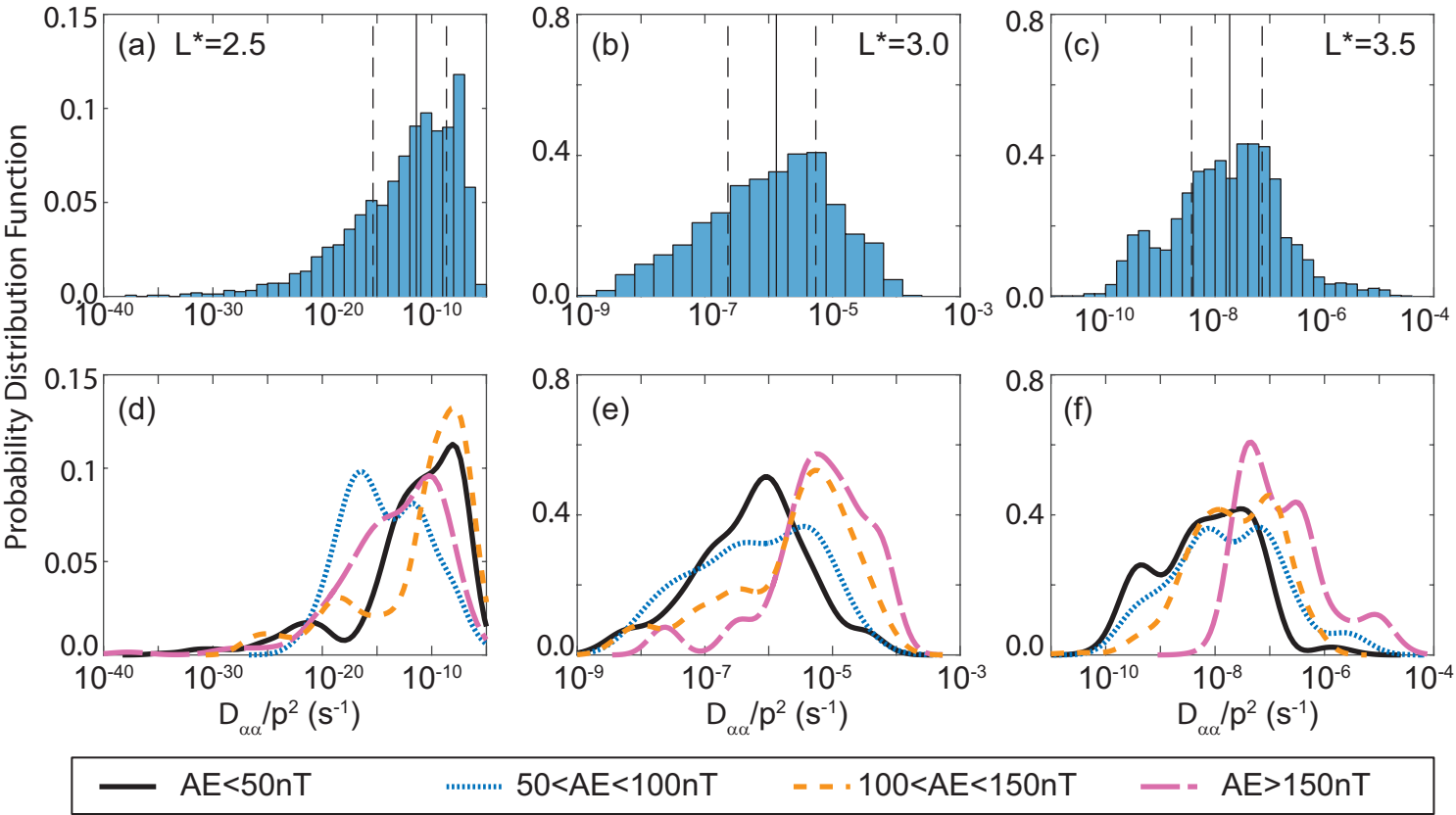
(a) L*=2.5
(b) L*=3.0
(c) L*=3.5
(d)
(e)
(f)
Probability Distribution Function
$D_{\alpha\alpha}/p^2$ (s^{-1})
AE<50nT
50<AE<100nT
100<AE<150nT
AE>150nT

Figure 8.

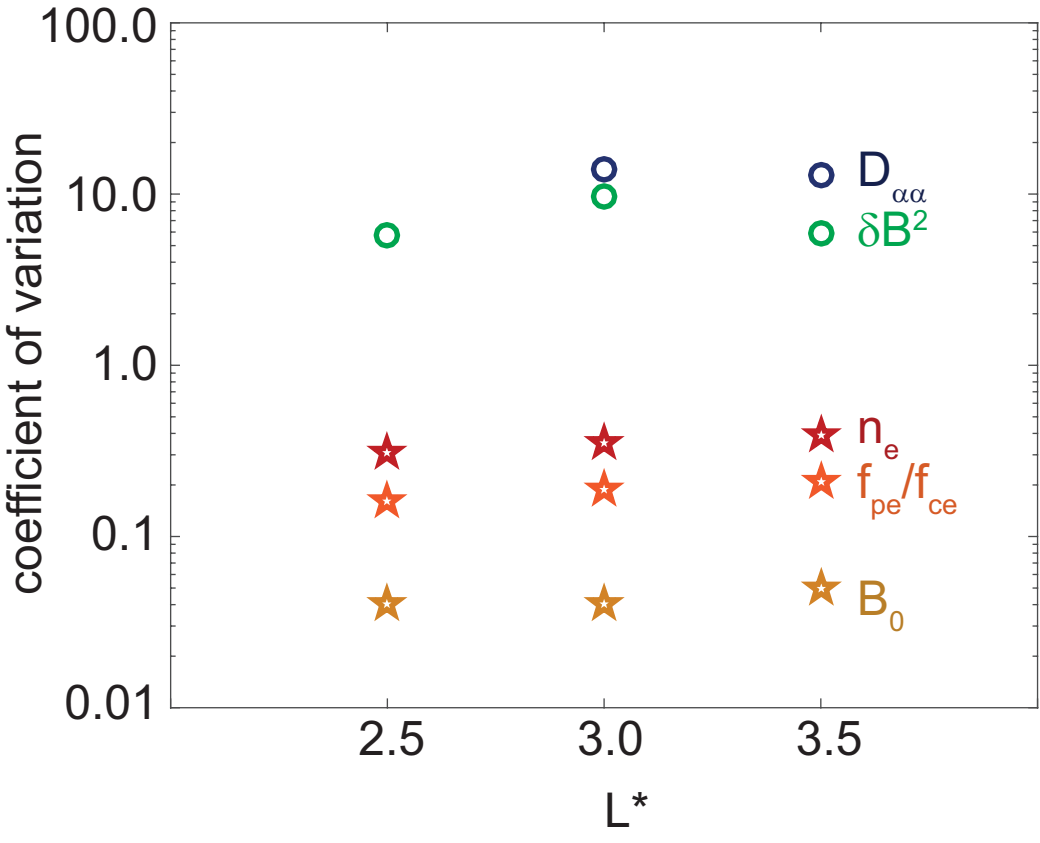
100.0
10.0
1.0
0.1
0.01
coefficient of variation
2.5
3.0
3.5
L*
$D_{\alpha\alpha}$
δB^2
n_e
f_{pe}/f_{ce}
B_0

Figure 9.

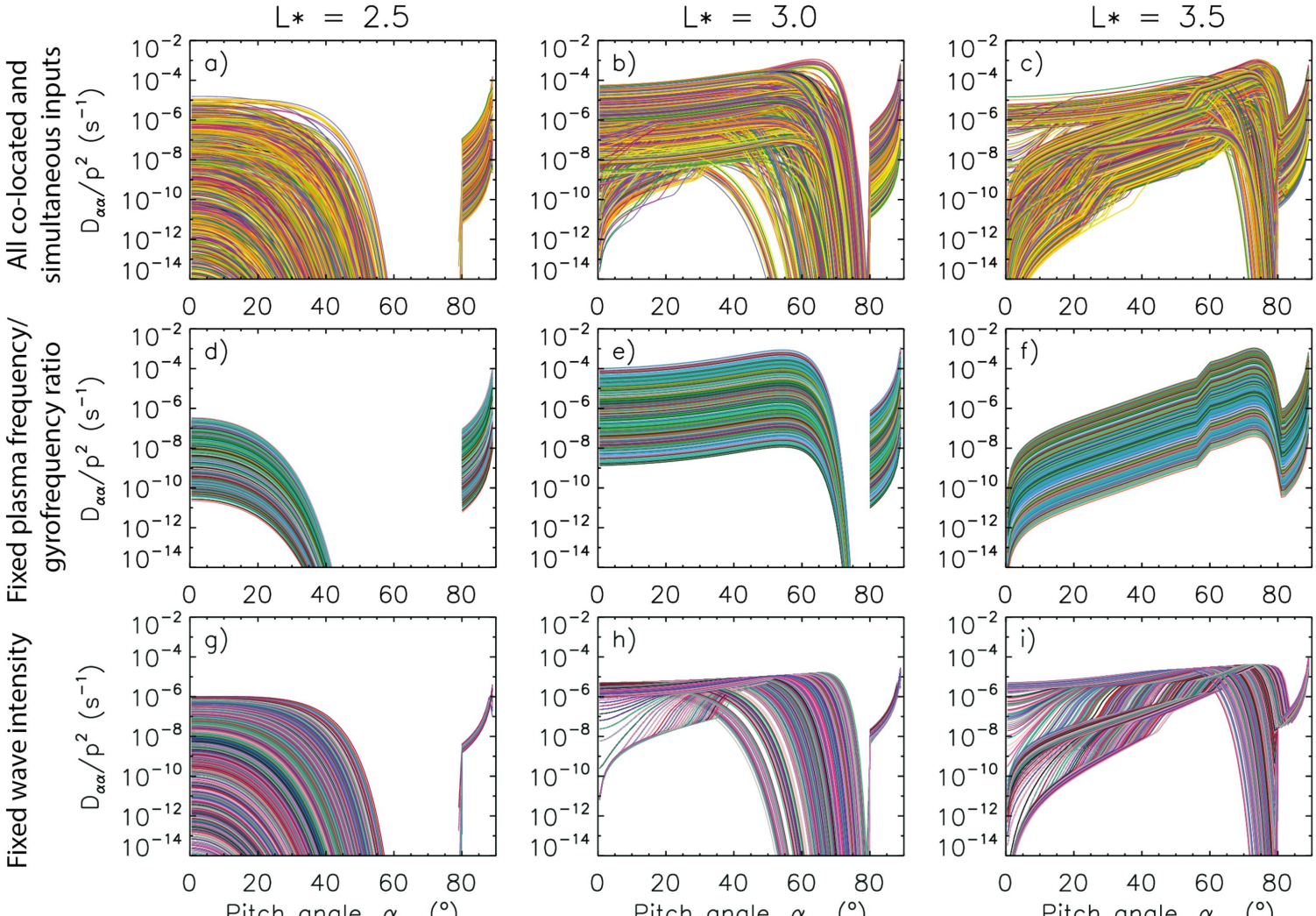
L* = 2.5
L* = 3.0
L* = 3.5
All co-located and simultaneous inputs
Fixed plasma frequency/ gyrofrequency ratio
Fixed wave intensity
$D_{\alpha\alpha}/p^2$ (s^{-1})
a)
b)
c)
d)
e)
f)
g)
h)
i)
Pitch angle, α_{eq} (°)

Figure 10.

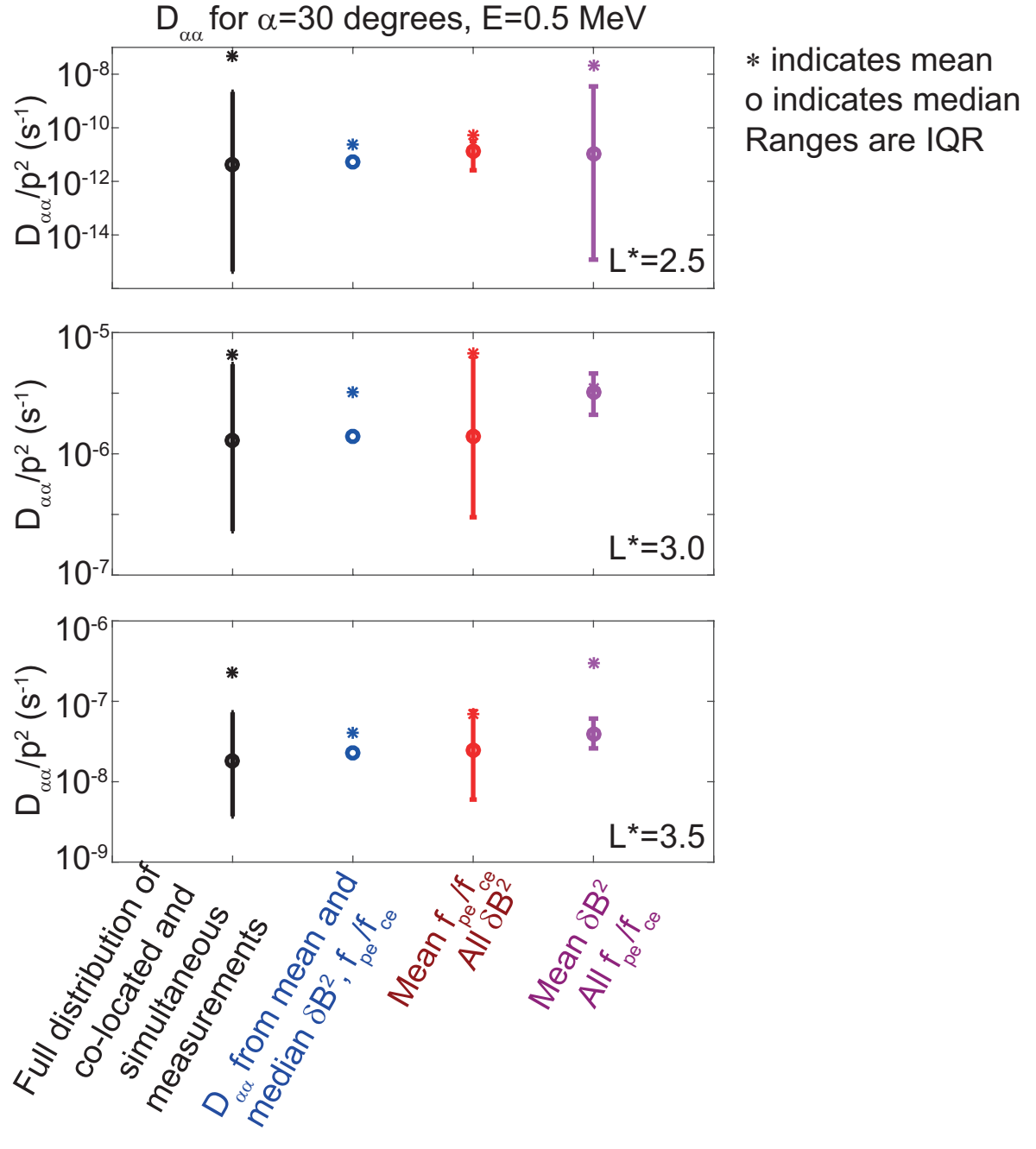
$D_{\alpha\alpha}$ for α=30 degrees, E=0.5 MeV
$D_{\alpha\alpha}/p^2$ (s^{-1})
10^{-8}
10^{-10}
10^{-12}
10^{-14}
L*=2.5
10^{-5}
10^{-6}
10^{-7}
L*=3.0
10^{-6}
10^{-7}
10^{-8}
10^{-9}
L*=3.5
∗ indicates mean
o indicates median
Ranges are IQR
Full distribution of co-located and simultaneous measurements
$D_{\alpha\alpha}$ from mean and median δB^2, f_{pe}/f_{ce}
Mean f_{pe}/f_{ce} All δB^2
Mean δB^2 All f_{pe}/f_{ce}